The choroid plexus links innate immunity to CSF dysregulation in hydrocephalus

Stephanie M. Robert[1,#], Benjamin C. Reeves[1,#], Emre Kiziltug[1,#], Phan Q. Duy[1,#], Jason K. Karimy[1], M. Shahid Mansuri[1,2,#], Arnaud Marlier[1], Garrett Allington[1,3], Ana B. W. Greenberg[1], Tyrone DeSpenza Jr.[1], Amrita K. Singh[1], Xue Zeng[1], Kedous Y. Mekbib[1], Adam J. Kundishora[1], Carol Nelson-Williams[1], Le Thi Hao[1], Jinwei Zhang[4], TuKiet T. Lam[2,5], Rashaun Wilson[2,5], William E. Butler[6], Michael L. Diluna[1], Philip Feinberg[7,8], Dorothy P. Schafer[7], Kiavash Movahedi[9,10], Allen Tannenbaum[11], Sunil Koundal[12], Xinan Chen[13], Helene Benveniste[12], David D. Limbrick Jr.[14], Steven J. Schiff[1], Bob S. Carter[6], Murat Gunel[1], J. Marc Simard[15,16,17], Richard P. Lifton[18], Seth L. Alper[19], Eric Delpire[20], Kristopher T. Kahle[6,21]

[1]Department of Neurosurgery, Yale School of Medicine; New Haven, CT, 06520, USA.

[2]Department of Molecular Biophysics and Biochemistry, Yale University School of Medicine; New Haven, Connecticut, 06520, USA.

[3]Department of Pathology, Yale School of Medicine; New Haven, CT, 06520, USA.

[4]Institute of Biomedical and Clinical Sciences, University of Exeter Medical School; Hatherly Laboratory, Exeter, EX1 2LU, UK.

[5]Keck MS & Proteomics Resource, Yale University School of Medicine; New Haven, Connecticut, 06520, USA.

[6]Department of Neurosurgery, Massachusetts General Hospital and Harvard Medical School; Boston, Massachusetts, 02114, USA.

[7]Department of Neurobiology, Brudnick Neuropsychiatric Research Institute University of Massachusetts Chan Medical School; Massachusetts, MA, 01655, USA.

Author Manuscript

[8]Medical Scientist Training Program, UMass Chan Medical School; Worcester, 01655, MA.

[9]Lab of Cellular and Molecular Immunology, Vrije Universiteit Brussel; Brussels, 1050, Belgium.

[10]Myeloid Cell Immunology Lab, VIB Center for Inflammation Research; Brussels, 1050, Belgium.

[11]Department of Applied Mathematics and Statistics, Stony Brook University, Stony Brook, NY, 11794, USA & Department of Medical Physics, Memorial Sloan Kettering Cancer Center, New York City, NY, 11794, USA.

[12]Department of Anesthesiology, Yale School of Medicine, New Haven, CT, 06520, USA.

[13]Department of Applied Mathematics and Statistics, Stony Brook University, Stony Brook, NY, 11794, USA.

[14]Department of Neurosurgery, Washington University School of Medicine; St. Louis, MO, 63110, USA.

[15]Department of Neurosurgery, University of Maryland, School of Medicine; Baltimore, Maryland, 21201, USA.

[16]Department of Pathology, University of Maryland, School of Medicine; Baltimore, Maryland, 21201, USA.

[17]Department of Physiology, University of Maryland, School of Medicine, Baltimore, Maryland, 21201, USA.

[18]Laboratory of Human Genetics and Genomics, The Rockefeller University; New York, NY, 10065, USA.

[19]Department of Medicine, Harvard Medical School; Boston, Massachusetts, 02115, USA.

[20]Department of Anesthesiology, Vanderbilt University School of Medicine; Nashville, Tennessee, 37232, USA.

[21]Broad Institute of Harvard and MIT; Cambridge, Massachusetts, 02142, USA.

SUMMARY

The choroid plexus (ChP) is the blood-cerebrospinal fluid (CSF) barrier and the primary source of CSF. Acquired hydrocephalus, caused by brain infection or hemorrhage, lacks drug treatments due to obscure pathobiology. Our integrated, multi-omic interrogation of post-infectious (PIH) and post-hemorrhagic hydrocephalus (PHH) models revealed lipopolysaccharide and blood-breakdown products trigger highly similar TLR4-dependent immune responses at the ChP-CSF interface. The resulting CSF "cytokine storm", elicited from peripherally-derived and border-associated ChP macrophages, causes increased CSF production from ChP epithelial cells via phospho-activation of the TNF receptor-associated kinase SPAK, which serves as a regulatory scaffold of a multi-ion transporter protein complex. Genetic or pharmacological immunomodulation prevents PIH and PHH by antagonizing SPAK-dependent CSF hypersecretion. These results reveal the ChP as a dynamic, cellularly heterogeneous tissue with highly regulated immune-secretory capacity, expand our understanding of ChP immune-epithelial cell crosstalk, and reframe PIH and PHH as related neuroimmune disorders vulnerable to small molecule pharmacotherapy.

Graphical Abstract
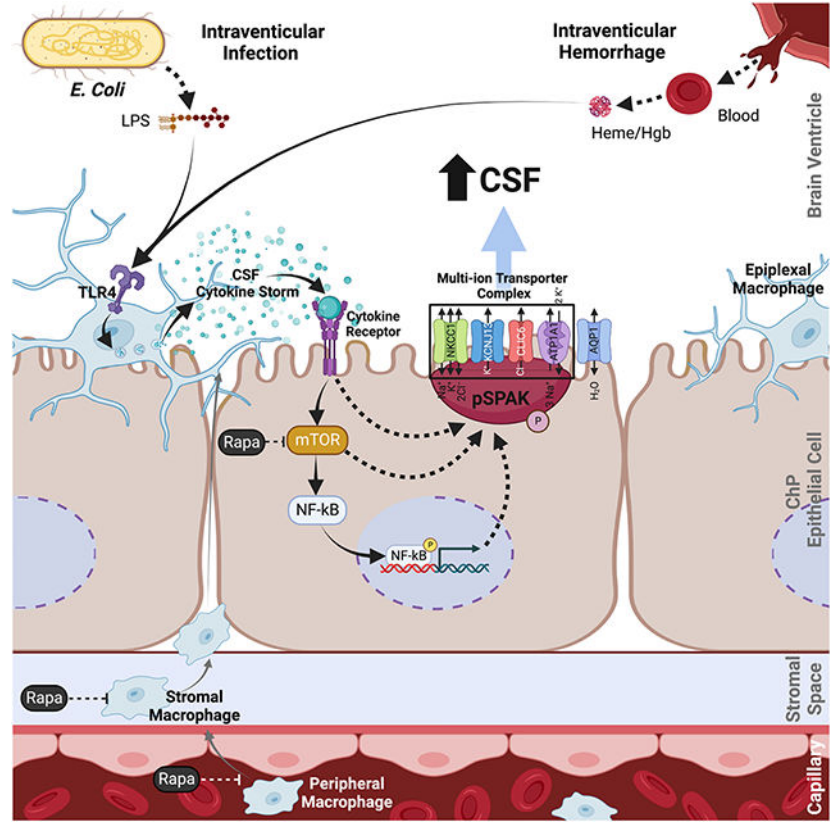
IN BRIEF

Infectious and hemorrhagic hydrocephalus converge on highly similar immune and secretory responses at the choroid plexus that drive pathological cerebrospinal fluid secretion, thus opening up immunomodulation as a potential non-surgical intervention.

INTRODUCTION

The choroid plexus (ChP) projects into each of the four cerebrospinal fluid (CSF)-filled ventricles and comprises an epithelial cell sheet populated by immune and mesenchymal cell types[1,2]. The ChP is the body's secretory epithelium *par excellence*, producing a half-liter of CSF per day via the concerted action of its multiple ion and water transport molecules[3]. The ChP is also the blood-CSF barrier, gating circulating immune cell entry into the CSF in the setting of infection or tissue damage[4-8]. The ChP's location at the nexus of the CSF, brain parenchyma, and systemic circulation allows it to sense perturbations and transduce danger signals into homeostatic responses. The cellular and molecular mechanisms that coordinate the immune and secretory functions of the ChP are poorly understood.

Hydrocephalus is characterized by the expansion of the cerebral ventricles (ventriculomegaly). Post-infectious hydrocephalus (PIH) and post-hemorrhagic hydrocephalus (PHH), the most common forms of hydrocephalus, are treated by

neurosurgical CSF diversion with or without ChP cauterization to decrease CSF production[9-11]. These life-saving operations have significant long-term morbidity and failure rates and are unavailable in impoverished areas[10,12,13]. ChP cauterization may also disrupt normal ChP functions important for brain development and immune function[14]. Drug treatments for hydrocephalus remain unavailable[14]. An improved understanding of ChP biology could identify therapeutic targets for hydrocephalus and other CSF disorders and neuroimmune diseases[4,8,14-17].

PIH and PHH are commonly attributed to intraventricular CSF accumulation secondary to decreased CSF reabsorption due to obstruction of intraventricular CSF flow and/or blockage of the extraventricular arachnoid granulations[18]. In contrast, the role of ChP's immune-secretory functions to the pathogenesis of hydrocephalus remains under-investigated. Interestingly, human PIH and PHH exhibit similar CSF profiles of immune cells and cytokines[19,20], and CSF neutrophilic pleocytosis can predict the development of PHH[21]. These observations suggest an important yet uncharacterized role of ChP and CSF space inflammation in the pathogenesis of acquired hydrocephalus.

Systemic epithelia respond to pro-inflammatory stimuli by increasing rates of fluid transport[22] to clear organisms or tissue debris[23-25]. However, inappropriately triggered or maladaptively sustained epithelial inflammation can dysregulate ion transport homeostasis. Examples include chemical, autoimmune, and infectious forms of pleuritis, colitis, and pancreatitis[25-28]. Intraventricular hemorrhage (IVH) is known to cause inflammation-induced ChP CSF hypersecretion in PHH models [29-33]. Nonetheless, the mechanism(s) by which the ChP contributes to PHH and PIH remain obscure, hindering the development of non-surgical treatment strategies.

Lipopolysaccharide (LPS)-expressing bacteria commonly cause PIH[34-36]. LPS is the canonical pathogen-associated molecular pattern (PAMP) for toll-like receptor-4 (TLR4)[37,38]. PHH-derived hemoglobin and possibly other blood products are TLR4-stimulating damage-associated molecular patterns (DAMPs)[39,40]. We hypothesized PIH and PHH have convergent pathophysiology that dysregulates ChP immune-secretory function. To test this, we created rat models of PIH and PHH and conducted a multi-omics investigation of these animals to dissect the physiologic, cellular, molecular pathology of PIH and PHH. Our results suggest that PIH and PHH are related neuroinflammatory disorders amenable to systemic immunomodulation.

RESULTS

E. coli post-infectious hydrocephalus models exhibit ChP-mediated CSF hypersecretion

Escherichia coli (E. coli) CSF infection is a common cause of post-infectious hydrocephalus (PIH) in resource-limited countries[34-36]. PIH is characterized by CSF space inflammation and the acute development of ventriculomegaly[10]. To investigate mechanisms of CSF infection on ChP function in PIH, we administered infectious material into the brain by intracerebroventricular (ICV) delivery. Wild-type E. coli (E. coli^{+LPS}) or E. coli genetically-engineered to lack LPS in the outer membrane (E. coli^{-LPS}, see Methods), were infused in sterile artificial CSF (aCSF) into the lateral ventricles of 8-week-old Wistar rats for

72h via stereotactically-placed infusion pumps (Fig. 1A). Control animals received ICV infusions of sterile aCSF. We found the lateral ventricular volume of animals 72h after infusion of *E. coli*[+LPS] was increased ~3-fold relative to control rats (Fig. 1, B and C). The ventriculomegaly in animals subjected to 72h ICV infusion of LPS alone (10 ng/μL in aCSF) resembled *E. coli*[+LPS]-treated animals (Fig. 1, B and C) and persisted when evaluated two weeks after treatment (fig. S1A). These findings suggest ICV-delivered LPS can model the acute development and persistence of ventriculomegaly characteristic of human PIH.

The pathways that regulate CSF homeostasis are poorly understood. However, acute ventriculomegaly in PIH could arise from impaired CSF efflux (e.g., due to obstruction of the cerebral aqueduct causing reduced bulk flow or reduced CSF egress via glymphatic and meningeal lymphatic pathways) and/or augmented CSF volume flux via an increase in ChP-dependent CSF production[41-43]. To examine CSF outflow in our PIH model, we injected the CSF tracer Evans Blue into the lateral ventricles of PIH rats after 72h of LPS infusion and found that dye distribution was unimpeded through the cerebral aqueduct and 4th ventricle, suggestive of aqueductal patency and preservation of bulk flow CSF (Fig. 1D). *In vivo* magnetic resonance imaging (MRI) of control and LPS-treated animals confirmed increased lateral ventricle volume in LPS-treated animals with normal intracranial volume (fig. S1, B-F), as well as cerebral aqueduct patency (fig. S1, G-H).

To examine glymphatic function in our PIH model, we performed *in vivo* dynamic contrast-enhanced, T1-weighted MRI after CSF infusion of gadoteric acid (see Methods)[44-46]. The MRI data were analyzed using computational fluid dynamics analysis based on regularized optimal mass theory which derives metrics describing the transport of the Gd-tagged contrast tracer in the brain[47]. Quantification of glymphatic v-flux (mm^3) and glymphatic mean tissue speed (mm/s) data revealed no significant differences in brain-wide glymphatic transport between LPS-treated and control animals (fig. S1, I-K). Notably, this nomenclature refers to 'glymphatic' transport because modeling included both diffusion and advection drivers for solute transport[47]. However, other perivascular transport models including the 'mixing model' and 'intra-mural periarterial drainage' (IPAD) have been proposed and will be considered in future studies[48-50]. While these results suggest PIH is associated with the development of acute, communicating ventriculomegaly, as is seen in many human patients[51,52], they do not exclude the possibility of alterations in CSF dynamics along other egress pathways[48].

We next directly measured the effect of LPS on the rate of CSF secretion using a validated method in live animals (Fig. 1E)[30,53,54]. In this method, mineral oil blocks CSF exit from the third ventricle at the level of the Sylvian aqueduct, preventing contributions to measured CSF secretion from CSF reabsorption pathways distal to this block (fig. S1L). Therefore, this technique measures *bona fide* lateral ventricle CSF production by the ChP[30,53,54]. LPS-treated PIH rats exhibited a >2.5-fold increase in CSF secretion relative to controls (Fig. 1E). A similar increase in CSF secretion was observed in *E. coli*[+LPS] hydrocephalic rats but not *E. coli*[−LPS] control rats (Fig. 1E). ICV infusion of aCSF in naive rats at a rate approximating the difference in CSF secretion rates between that of control rats and LPS-induced or *E. coli*[+LPS] hydrocephalic rats recapitulated the ventriculomegaly observed in both conditions. ICV-delivered bumetanide, an inhibitor of ChP-mediated CSF secretion[30,55,56], reduced

LPS-induced CSF secretion by >70% (Fig. 1E). LPS-induced CSF hypersecretion and ventriculomegaly were attenuated in *Tlr4* knockout rats (*Tlr4*$^{-/-}$)[57] (Fig. 1, F-H). These results suggest acute ventriculomegaly in PIH models results from an LPS-triggered, TLR4-dependent increase in bumetanide-sensitive CSF secretion from the ChP.

Post-infectious hydrocephalus models are associated with robust ChP-CSF interface inflammation

To gain molecular insight into the observed ChP-mediated acute CSF hypersecretory response in our models of PIH, we generated transcriptomic and proteomic datasets of micro-dissected lateral ventricle ChP from LPS-induced hydrocephalic and control rats using bulk RNA-sequencing and quantitative mass spectroscopy (Fig. 2A). Differential expression analyses of RNA transcripts (Fig. 2B, genes) and polypeptides (Fig. 2C, proteins) revealed significant differences between LPS-treated and control ChP. Wiki pathway, Gene Ontology (GO), and Mouse Gene Atlas analyses of the top 100 differentially-expressed genes and proteins in PIH versus control animals revealed enrichment of terms related to innate immunity and inflammation, such as "positive regulation of myeloid leukocyte mediated immunity" and "microglia pathogen phagocytosis pathway" (Fig. 2, D and E, and Table S1).

We next integrated our bulk multi-omics ChP data with published single-cell and single-nucleus RNA-sequencing (sc- and snRNAseq, respectively) of the ChP and brain macrophages[2,58]. We constructed 21 modules of co-expressed genes from a published scRNAseq dataset of rodent ChP[58] (Fig. 2F) and found that PIH-associated transcripts converged within a single module associated with monocytes that included dendritic cells (cDC1s, cDC2s, and migDCs) (Module 11, Fig. 2G)[59]. The most upregulated transcripts and proteins in PIH converged in another immune cell-specific co-expression module (Module 17, Fig. 2G)[59]. Genes in Modules 11 and 17 were both significantly enriched in pathways related to the recruitment of circulating myeloid/lymphoid cells and chemokine/interferon receptor signaling, as well as ChP secretory activity including chloride ion binding and ligand-gated ion channel activity (Fig. 2H, Table S1).

Multiple cytokines responsible for inflammatory cell signaling and modulation, and multiple chemokines responsible for the recruitment of circulating myeloid and lymphoid cells, were significantly increased in the CSF of LPS-treated animals compared to controls (Fig. 2I and fig. S1M). Among these, the most highly up-regulated (>30-fold increase, p=0.0017) was C–C motif chemokine ligand 2 (Ccl2). Levels of Ccl5 and C-X-C motif ligand 5 (Cxcl5), tumor necrosis factor-alpha (Tnfα), Il-1ß, Il-6, and other interferons and interleukins were also significantly increased. These findings indicate that CSF of PIH animals exhibits a pro-inflammatory state absent from normocephalic (non-hydrocephalic) control animals and similarly treated *Tlr4*$^{-/-}$ rats (Fig. 2I).

LPS-treated animals demonstrated accumulation and proliferation of Iba1$^+$ macrophages at the apical, CSF-facing ChP surface and ChP stromal compartment between the basolateral membrane and endothelium (Fig. 2, J-N). Iba1$^+$ cells likely include immune cells recruited from the periphery[4,58] and CNS border-associated macrophages (BAMs), consisting of epiplexal (Kolmer) and stromal subtypes. In contrast to their quiescent appearance in

controls[58], BAMs in PIH rats exhibited amoeboid-like shape, increased circularity (Fig. 2, J and K)[60], and increased CD68/ED1-positivity (Fig. 2, K and M), all indicative of increased phagocytic activity[61]. ChP-associated Iba1^{+} and CD68/ED1^{+} cells were reduced in similarly treated $Tlr4^{-/-}$ rats (Fig. 2, K-N). In comparison to $E.\ coli^{+LPS}$-treated animals, the ChP of $E.\ coli^{-LPS}$ rats exhibited a milder inflammatory reaction (fig. S2, A-C). Like human patients with PIH[62-65], $E.\ coli^{+LPS}$-treated animals, and to a lesser extent $E.\ coli^{-LPS}$ animals, also exhibited immune cell activation in the meninges lining the CSF spaces and cortex (fig. S2).

Fluorescence-activated cell sorting (FACS) of micro-dissected, dissociated lateral ventricle ChP labeled with an antibody against CD45, a glycoprotein that marks immune cells of peripheral origin[66,67], revealed higher CD45^{+} cell numbers in the ChP of PIH animals than of controls (Fig. 2, O and P, left panels). CD3^{+} T-cell number was also increased (Fig. 2, O and P, right panels). LPS-mediated increases in ChP-associated CD45^{+} peripheral immune cells and CD3^{+} T cells were attenuated in $Tlr4^{-/-}$ animals (Fig. 2, O and P). These data suggest PIH is associated with TLR4-dependent accumulation and activation of peripherally-derived immune cells and resident BAMs at the ChP that elicit a robust innate immune response characterized by a "CSF cytokine storm." This is consistent with the ChP-CSF-brain interface inflammation in patients with PIH and other forms of acquired hydrocephalus[65,68-70].

SPAK kinase links pro-inflammatory CSF cytokine signaling to ChP-mediated CSF secretion

Analysis of ChP snRNAseq results[2] (fig. S3, A-E) revealed high baseline $Tlr4$ expression in ChP-associated macrophages and myeloid lineage immune cells, but scant expression in ChP epithelial cells (fig. S3B). Expression profiles of immune-related genes in adult ChP epithelial cells further revealed 3 unique subclusters (Table S2), all with low-level $Tlr4$ expression. In contrast, even under basal conditions, ChP epithelial cells exhibited significant levels of expression for multiple receptors of pro-inflammatory cytokines upregulated in CSF of PIH animals (Fig. 2I) and humans[20], including TNFα, IL1ß, IL6, CCL2, and IFNγ. We hypothesized CSF cytokines elaborated by activated immune cells at the ChP stimulate their receptors on ChP epithelial cells to promote CSF secretion. Consistent with this hypothesis, quantitative real-time PCR of micro-dissected ChP epithelial cells showed higher expression of $Ccr2$, $Relt$, and $Il1r1$ in LPS-treated animals than in controls (fig. S3F). The Tnfα receptor Relt was also significantly up-regulated at the apical membrane in PIH rats, but not in similarly-treated $Tlr4^{-/-}$ rats (fig. S3, G and H).

The bumetanide-sensitivity of the acute CSF hypersecretory response in PIH implicates the NKCC1 cotransporter in disease pathogenesis. NKCC1 phosphorylation at Thr203, Thr207, and Thr212 by SPAK kinase is required for NKCC1 activity[71]. SPAK phosphorylation at Ser373 by WNK1 kinase is required for SPAK kinase activity[72]. SPAK transduces extracellular stress signals, including NF-κB-dependent cytokines, into downstream signaling events[73]. RELT binds SPAK via its C-terminal domain[74] and TNFα and IL-1β stimulate SPAK kinase activity in a TLR4- and NF-κB-dependent manner to increase intestinal epithelial transport[25,73]. We hypothesized SPAK transduces TLR4-dependent pro-

inflammatory CSF signals into a ChP epithelial CSF hypersecretory response by increasing NKCC1 phosphorylation.

Consistent with SPAK functioning downstream of TLR4-mediated immune cell activation in a non-cell-autonomous manner, expression of *Spak* and *Nkcc1* in ChP epithelial cells far exceeded that in other ChP cell types (fig. S3, I and J). The phosphorylated, activated species of SPAK (pSpak) and NKCC1 (pNkcc1)[71,72,75,76] were up-regulated at the ChP apical membrane in PIH rats but not in similarly treated *Tlr4*^{−/−} rats (fig. S3, K-M). While *Spak* knockout had no effect on LPS-induced increases in ChP-associated immune cell infiltration and activation or Relt expression (fig. S4, A-B)[77], it prevented the up-regulation of pSpak-pNkcc1 in ChP epithelial cells (fig. S3, K-M) and attenuated LPS-induced increases in CSF secretion and ventriculomegaly (fig. S3, N and O). These data suggest SPAK mediates molecular crosstalk between TLR4-dependent ChP immune cell activation and NKCC1-dependent CSF secretion by ChP epithelial cells via cytokine receptor engagement.

SPAK is a regulatory scaffold of a multi-ion transporter complex at the ChP apical membrane

CSF secretion requires the coordinated function of multiple ion and water transport proteins (Fig. 3A)[3,56]. NKCC1 is the canonical SPAK target; however, SPAK regulates multiple ion transport proteins[26]. To investigate whether other ion transporters are involved in the SPAK-dependent CSF hypersecretory response, we immunoprecipitated SPAK from micro-dissected ChP of adult *Spak*^{−/−} and *Spak*^{+/+} rats, and adult pigs (a model with increased ChP volume per animal) and analyzed the composition of immunoprecipitates using LC-MS-MS (Fig. 3B)[30]. Spak was the most abundant protein in the purified immune complexes from wild-type pig and rat ChP but absent from *Spak*^{−/−} ChP. Nkcc1, the Na$^+$/K$^+$ ATPase α-1 subunit Atp1a1, the Cl$^-$ channel regulatory protein Clic6, the K$^+$ channel Kcnj13, and Wnk1 were among the most significantly enriched Spak-bound proteins in immunoprecipitates from wild-type pig and rat ChP (Fig. 3C). These proteins were absent from *Spak*^{−/−} ChP immunoprecipitates. Pulldown experiments validated these findings (Fig. 3D).

snRNAseq analysis of ChP epithelial cells showed high expression of *Wnk1*, *Stk39* (Spak), *Slc12a2* (Nkcc1), *Atp1a1*, *Kcnj13*, and *Clic6* in each ChP epithelial cell subcluster at levels significantly higher than other ChP cell types (fig. S4C). Spak co-localized with Atp1a1, Kcnj13, and Clic6 at the ChP apical membrane (Fig. 3E). PIH rats had increased *Tlr4*- and *Spak*-dependent co-localization of all three apical transporters, as well as of water channel Aqp1, with pSpak at the ChP apical membrane (Fig. 3E). These findings suggest SPAK is both a transducer of immune signals and regulator of ion transporters that are integral to PIH pathophysiology in ChP epithelial cells.

Post-infectious and -hemorrhagic hydrocephalus share common ChP immune-secretory mechanisms

Intraventricular organisms in PIH and blood products in PHH are similarly associated with CSF immune cell infiltration and cytokine production in patients [19,78,79]. Bacteria-derived LPS and autologous blood products (e.g., heme) are well-known TLR4

pathogen-associated molecular patterns (PAMPs) and damage-associated molecular patterns (DAMPs), respectively[80,81]. We hypothesized convergent pathophysiology affecting ChP immune-secretory capacity drives the development of acute ventriculomegaly in both PIH and PHH.

To test this, we generated transcriptomic and proteomic datasets of micro-dissected lateral ventricle ChP from a validated rat model of intraventricular hemorrhage (IVH)-induced PHH[30] and control rats. The PHH model resembles the PIH model, except that blood from the tail vein is harvested and injected directly into the lateral ventricles of the same animal (see Methods). Comparison of the PHH datasets with those from age- and sex-matched PIH rats revealed a striking overlap of the most differentially-expressed genes and proteins (Fig. 4, A-D and Table S3). Highly enriched pathways were related to macrophage-mediated innate immunity, toll-like receptor signaling, cytokine receptor transduction, and phosphoinositide 3-kinase signaling (Fig. 4, D-F and Table S3).

Integrated analysis of the top differentially expressed genes and proteins in PHH with scRNAseq data showed convergence to the same immune cell-specific co-expression module identified in PIH (Module 17, Fig. 4, E and F, and Table S3). Like PIH rats, PHH rats exhibited increased Iba1+, ED1+, and Ki67+ ChP-associated macrophages (Fig. 4, G and H) and *Tlr4*-dependent increases in CD45+ and CD3+ T-cells at the ChP (Fig. 4, I and J). PHH also rats resembled PIH rats in their >2-fold increased *Tlr4-* and *Spak*-dependent ventriculomegaly (Fig. 4K); >2-fold increased CSF hypersecretion (Fig. 4L); and up-regulated pSpak-pNkcc1 apical membrane ChP expression (Fig. 4, M-O). These results show PIH and PHH share a pathophysiological signature characterized by TLR4-mediated ChP immune cell signaling and SPAK-dependent ChP transepithelial ion transport.

scRNAseq uncovers molecular crosstalk between peripherally-derived and resident immune cells and ChP epithelial cells

Given the similarities of the ChP immune response to LPS and IVH, we performed single-cell RNA sequencing (scRNAseq) on microsurgically-dissected ChP (Fig. 5A) from control, PIH, and PHH animals (Fig. 5). We then compared the CD45+ and CD45− cell expression profiles (Fig. 5, B and I) using markers (Fig. 5C and fig. S5A) defined in the literature[2,58]. The integrated CD45+ dataset consisted of 1427 control, 3331 PHH, and 5529 PIH ChP immune cells. The integrated CD45− dataset consisted of 2036 control, 718 PHH, and 1603 PIH ChP non-immune cells. Clustering of CD45+ immune cells in control ChP resembled findings previously reported[58].

Comparing CD45+ immune cells in the ChP from PIH and PHH animals demonstrated significantly different immune cell profiles compared to control. However, the inflammatory profiles of the ChP from PIH and PHH animals closely resembled each other (Fig. 5B and D), with similar increases in macrophage/monocytes and neutrophils (Fig. 5B and E). Heatmap analysis of the most differentially expressed genes in the CD45+ dataset showed highly significant overlap for PIH and PHH compared to control (Fig. 5D). Interestingly, plasmacytoid DCs (pDCs) and CD4+ T cells were particularly increased in PIH (Fig 5B and E).

The myeloid cell population was further separated into three main subclusters, in agreement with recently defined markers[58], which included stromal BAMs (CP_BAM; C1qa[hi]Csf1r^{hi}Cd14^{lo}), ChP-epiplexus cells (CP_Epi; Sall1^{+}), and peripherally-derived blood monocytes (Pbm, Cd14^{hi}C1qa[lo]) (Fig. 5, F and G). The Pbm sub-cluster was increased in the ChP from PIH and PHH compared to control, reflecting the infiltration of peripheral macrophages (Fig. 5, F and G)[58]. As top markers of the Pbm-2 subcluster included interferon-stimulated genes (such as Irf7 Isg15, Isg20, Ifit2, Ifit3 and Ifitm3), Pbm recruitment is likely a response to upregulated interferon signaling.

The significant increase in Pbm, neutrophils, and pDCs in the ChP of PIH and PHH animals prompted pathway analyses of the top markers for these cell populations (fig. S5, B-J). Pbm pathway analysis revealed enrichment of pathways related to macrophage function and chemokine/interferon signaling, macrophage and neutrophil chemotaxis and migration, and regulation of dendritic differentiation (fig. S5B). Neutrophil pathway analysis showed enrichment of interferon/chemokine signaling and PI3K-Akt-mTOR signaling pathways (fig. S5D). pDC pathway analysis also identified significant enrichment of TLR signaling, chemokine signaling, and PI3K-Akt-mTOR signaling pathways (fig. S5, E and F).

The ChP epiplexus macrophage (Kolmer cells) cell population transformed similarly in PIH and PHH ChP compared to controls (Fig 5F). When further subclustered, both PIH and PHH exhibited two new populations of ChP-associated Kolmer cells (Fig 5H, blue and green). Pathway analysis revealed enrichment of DNA replication and mitotic division processes in sub-cluster 1 (fig. S5G), suggesting a subpopulation of replicating Kolmer cells. Pathway analysis for top markers of Kolmer cell sub-cluster 2 showed enrichment of LPS-mediated signaling, TLR signaling, and chemokine receptor binding, among others (fig. S5H).

Clustering of the ChP CD45^{−} non-immune cell populations demonstrated findings like those previously reported (Fig 5I)[2]. Heatmap analysis of the most differentially expressed genes in the CD45^{−} dataset again revealed substantial overlap for PIH and PHH ChP compared to control ChP (Fig. 5J). Subclustering of the epithelial cell (CD45^{−}) population uncovered a new ChP epithelial subcluster in PIH and PHH (Fig. 5K; subcluster 2), which expressed *Cxcl17*, *CxcI9*, *Ccl5*, *Il18bp*, and *Irf7* (Table S4, fig. S6). Inflammatory and immune signaling pathways, particularly type I interferon signaling, were enriched in this subcluster in both PIH and PHH (fig. S5, I and J).

To compare ligand-receptor interactions in control, PIH, and PHH animals, we merged the CD45^{+} and CD45^{−} datasets and applied CellChat[82], a scRNAseq tool used for inferring intercellular communication networks based on the expression of known ligand-receptor pairs in different cell clusters (Fig. 6A). Our analysis identified 6 ligand-receptor pathways present in both PIH and PHH ChP that were absent in the control ChP (Fig 6B). Among these, the Osteopontin (Spp1) ligand-receptor pathway showed very similar ligand-receptor interaction profiles for both PIH and PHH ChP (Fig 6C). In both groups, the most significant ligand-receptor interactions originated from ChP epiplexus macrophages to ChP resident macrophages, monocytes, T cells, B cells, and DCs (Fig 6C). CellChat analysis also identified the ligand-receptor pairs Spp1-Cd44 and Spp1-(Itga4_Itgb1) as the most

significant signaling contributing to the Spp1 communication pathway (Fig 6D). These interactions are known to activate the PI3K-Akt-mTOR signaling pathway[83,84].

We next examined ligand-receptor signaling pathways present in all three conditions but independently upregulated in PIH or PHH ChP compared to the control ChP. Cell-cell communications were very similar for PIH and PHH, showing significant upregulation in inflammatory pathways including MHC-I, CCL, CXCL, and FN1 (Fig 6E). We then compared the ligand-receptor signaling pathways of epithelial and immune cells in PIH and PHH ChP to control ChP. We found inflammatory and cell adhesion pathways such as chemokine (CXCL), Galectin, and Periostin to be activated in both PIH and PHH ChP between epithelial and immune clusters (Fig 6F). The significant CXCL interactions between ChP epithelial and immune cells were mainly sent from epithelial cells to T cells and to dendritic cells for both PIH and PHH compared to control (Fig 6G). Cell-cell communication analysis revealed that ligand-receptor pairs *Cxcl11-Cxcr3* and *Cxcl9-Cxcr3* contributed most significantly to the CXCL epithelial-immune cell communication pathway (Fig 6H) in both PIH and PHH, suggesting that ChP epithelial cells play active roles during the inflammatory response.

Repurposed systemic immunomodulators treat hydrocephalus by antagonizing ChP-mediated CSF hypersecretion

The importance of highly similar ChP immune-secretory mechanisms to the development of acute ventriculomegaly in PIH and PHH suggested the possibility of shared therapeutic strategies. No clinically approved drugs target TLR4 or SPAK, but multiple agents are in clinical trials or in preclinical development[42,85,86]. We therefore mined our ChP -omics data for pathways enriched in both PIH and PHH models that are targeted by clinically approved drugs. Among top-ranked hits, the PI3K-Akt-mTOR-signaling pathway (WikiPathways WP2841; z-score 12.13) (Fig. 2E) was an appealing target because of its role in both immune cells and SPAK activation[87-89]. Indeed, the top differentially expressed genes and proteins common to PIH and PHH were enriched in multiple phosphatidylinositol pathways, the most significant of which was 1-phosphatidylinositol-3-kinase regulator activity (GO: 0046935; z-score 141.43) (Fig. 4, D and F)[90]. Integration of differentially expressed genes with published scRNAseq data revealed enrichment of the Focal Adhesion-PI3K-Akt-mTOR-signaling pathway (WP2841) in co-expression module 11 (z-score 4.16) (Table S1). Consistent with these findings, phosphorylation of S6 ribosomal protein (pS6), indicative of mTOR pathway activation, was significantly increased in both ED-1+ ChP immune cells and ChP epithelial cells in both PIH and PHH rats, but not in similarly treated *Tlr4*^{−/−} rats (Fig. 7A). snRNAseq analysis revealed high *Mtor* and *Nfkb* expression in ChP epithelial cells and hematopoietic cells (Fig. 7B and fig. S7, A-B). These results suggest PI3K/Akt/mTOR signaling is a therapeutic target in PHH and PIH.

We tested the hypothesis that systemic treatment with rapamycin, an immunosuppressive mTOR inhibitor, would attenuate the development of acute PIH and PHH by antagonizing inflammation-dependent CSF hypersecretion from ChP epithelial cells. In both PIH and PHH rats, intraperitoneal rapamycin (6 mg/kg administered 2-3h prior to initiating LPS infusion or 2-3h pre-IVH) decreased up-regulated pS6 immunostaining in ChP immune cells

and epithelial cells (Fig. 7A), reduced numbers of ChP-associated Iba1^{+}, ED1^{+}, and Ki67^{+} cells (Fig. 7, C-F), and attenuated the LPS- and IVH-induced influx of CD45^{+} cells (Fig. 7G). Rapamycin also attenuated both LPS- and IVH-induced increases in CSF secretion (Fig. 5H), ventriculomegaly (Fig. 7I and fig. S7, C-E), and pSPAK-pNKCC1 abundance at the ChP apical membrane (Fig. 7, J-L). Strikingly, delay of rapamycin administration until 3 h after initiating LPS infusion had similar effects, including attenuation of LPS-mediated ventriculomegaly (fig. S7, C-E) and a decrease in ChP-associated Iba1^{+} and ED1^{+} cells (fig. S7, F-G). These results suggest that repurposed systemic immunomodulators can ameliorate acute PIH and PHH by antagonizing ChP epithelial cell CSF hypersecretion.

DISCUSSION

Results from multi-modal analysis of CSF dynamics in *E. coli* models of PIH suggest that acute ventriculomegaly results primarily from an LPS-induced increase in ChP CSF secretion. These data may revise or augment existing paradigms emphasizing obstruction of intraventricular CSF flow. The relevance of these findings is supported by observations in patients that: (i) PIH can develop within hours of CNS infection[91] and can precede radiographic evidence of aqueductal obstruction[92]; (ii) destruction of the ChP (with or without an endoscopic third ventriculostomy [ETV]), can effectively treat PIH[93] and some other forms of hydrocephalus; and (iii) increased CSF secretion can cause hydrocephalus in humans with ChP hyperplasia in the setting of ChP tumors[94-96] and certain genetic syndromes[97-100]. Although multiple models of CSF clearance have been proposed (e.g., via vascular basement membranes, the intramural periarterial drainage pathway, perineuronal routes, and skull base lymphatics), their role in hydrocephalus, particularly in chronic hydrocephalus when inflammation-dependent scarring from tissue damage could impact resorptive mechanisms[101,102], will be important topics of future investigation.

While we demonstrated that LPS, likely *E. coli*'s most immunogenic virulence factor, is necessary and sufficient to cause CSF hypersecretion and ventriculomegaly in our PIH model, the full immune response to *E. coli* at the ChP-CSF interface likely includes components besides LPS, such as flagellar H-antigens and capsular K-antigens[103,104]. Indeed, animals treated with LPS-deficient *E. coli*[–LPS] still exhibit ChP-CSF interface inflammation, albeit less severe than with *E. coli*[+LPS], and exhibit a trend towards ventricular enlargement [105,106]. Moreover, the immune response to *E. coli* and to other infectious agents impacts the meninges and parenchyma[105,106]. Future studies will explore the involvement of other portals of immune cell entry into the brain and whether PAMPs from other PIH-causing bacteria (e.g., the TLR5 agonist flagellin[107]) trigger ChP CSF hypersecretion.

Our data supports BAMs on the apical ChP membrane as the "first responders" to microorganisms in the CSF[108-111]. ChP macrophages express TLRs, which bind PAMPs to activate innate immune responses[111,112]. Our integrated -omics analysis showed dependence of the acute ChP hypersecretory response in PIH on LPS-induced, TLR4-mediated recruitment of both peripheral blood monocytes and accumulation, proliferation, and activation of resident stromal BAMs (C1qa[hi]Csf1r^{hi}Cd14^{lo}) and ChP-epiplexus macrophages (CP_Epi, Sall1^{+}). A similar TLR4-dependent immune cell response was triggered in

PHH by intraventricular hemorrhage-derived DAMPs such as heme[40,80,113,114]. Notably, ChP macrophage depletion attenuates ventriculomegaly following ICV-injection of the proinflammatory blood product peroxiredoxin-2[115]. These data show the remarkable similarity of the innate immune cell responses to CNS infection and to hemorrhage, and highlight the ChP as a dynamic, cellular heterogeneous tissue with highly regulated immune-secretory capacity.

We found acute PIH and PHH are both characterized by a CSF "cytokine storm" analogous to sepsis-associated elevations of blood circulating cytokines in the settings of systemic infection or widespread tissue damage[116,117]. These observations correspond to cytokine and immune cell responses in human CSF stimulated by intraventricular infection and hemorrhage[19,78,79]. CSF cytokines likely engage their cognate receptors on ChP epithelial cells to modulate epithelial cell function. Among up-regulated cytokines, Ccl2 and its ChP epithelial cell receptor Ccr2 recruits macrophages to the ChP-CSF interface in response to maternal immune activation [4]. The ChP's ability to detect infection or tissue damage and initiate a counter-response may also be an Achille's heel that renders the brain susceptible to attack by circulating immune cells in multiple sclerosis and other diseases[8,118,119].

SPAK kinase links ChP immune cell signaling and epithelial function via its interactions with upstream cytokine receptors and downstream ion transport proteins[73]. The TNF-α receptor RELT binds SPAK to regulate the innate immune system[74] and increase epithelial transport in experimental inflammatory bowel disease[73,120,121]. SPAK is a master regulator of the *SLC12A* family cation-Cl⁻ cotransporters such as NKCC1[122]. SPAK phospho-activation in the ChP, triggered by LPS or IVH, leads to increased ChP CSF production in part by phosphorylating and thereby stimulating NKCC1. These data accord with the importance of bumetanide-sensitive (NKCC1-mediated) ChP transport for CSF production in humans[123], dogs[55], rats[30], and mice[124], and are consistent with the finding that patients with loss-of-function NKCC1 mutations exhibit decreased epithelial secretion and "slit-ventricle" brain morphology indicative of decreased intraventricular CSF volumes[125].

NKCC1 operates close to its equilibrium electrochemical potential in the ChP as in other epithelia. This suggests the capacity for regulated, bidirectional net ion and fluid transport across the ChP[75,124] and might account for reported differences in the vector of NKCC1-mediated net ion transport (inward vs. outward), and in net CSF secretion and/or CSF clearance in various developmental[126] and/or disease contexts[30]. We showed Spak binds not only Nkcc1[122,127], but also other ion transport proteins implicated in CSF secretion including Atp1a1. We predict that SPAK functions as a regulatory scaffold that senses extracellular and/or intracellular signals (e.g., changes in CSF ionic composition), and then transduces these signals into phosphorylation events to coordinate the activities of an ensemble of associated ion transport proteins.

Drugs targeting TLR4 or SPAK have not been clinically approved[42,128,129]. Our -omics data converged upon PI3K-Akt-mTOR signaling as important for ChP immune-secretory mechanisms in both PIH and PHH, consistent with this pathway's contributions to immune cell and epithelial cell homeostasis[130], and to TLR4[131,132] and SPAK signaling[88,133]. "Rapalog" mTOR inhibitors are approved for systemic treatment of allograft rejection and

for adjunct treatment of subependymal cell astrocytomas[134,135]. The immunosuppressive effects of mTOR inhibition likely prevail over other growth-mediated pathways in rapamycin's therapeutic effect on our acquired hydrocephalus models. Other potential beneficial effects of rapamycin may include its autophagy-inducing effects in brain microglia[136] and inhibition of hypoxia-inducible factor 1a[137]. The clinical utility of rapamycin will be better assessed by testing later time points of administration. Repurposed drugs modulating ChP immune-secretory function might be a viable non-surgical treatment strategy for multiple forms of acquired hydrocephalus and for other neuroimmune brain disorders associated with ChP dysfunction.

Limitations of the Study

Limitations of our study include our reliance on the rat as a model organism, chosen for its amenability to *in vivo* measurements of CSF secretion and for its CSF volume higher than that of mouse. Future development of non-invasive, imaging-based assays to measure ChP-mediated CSF production, and of ChP-specific gene targeting approaches should overcome present limitations of our direct surgical CSF secretion assay and of current indirect methods to interrogate *in vivo* transporter activity. Additional limitations include the lack of correlative scRNAseq analysis of CSF from PIH and PHH patients, and lack of clinical data testing efficacy of rapamycin and other immunomodulators as treatments for hydrocephalus. The latter could be studied in patients with high-grade aneurysm rupture complicated by intraventricular hemorrhage and PHH, all currently managed with indwelling intraventricular drains and intermittent imaging.

STAR METHODS

RESOURCE AVAILABILITY

Lead Contact—Requests for further information should be directed to and will be fulfilled by the Lead Contact, Kristopher Kahle (kahle.kristopher@mgh.harvard.edu).

Materials Availability—Mouse lines generated in this study have been deposited to the Knockout Mouse Project (KOMP), Charles River, albino wister rats, strain code 003.

Data and Code Availability

- Single-cell RNA-seq data have been deposited at GEO and are publicly available as of the date of publication. Accession numbers are listed in the key resources table. The mass spectrometry proteomics data have been deposited to the ProteomeXchange Consortium via the PRIDE[139] partner repository with the dataset identifier PXD030678. Any FACS or microscopy data, confocal, or other, reported in this paper will be shared by the lead contact upon request. All materials and associated protocols can be found within the methods section of this paper, and any relevant papers are also cited for further reference. In addition to the methods provided here, for additional explanations of the IVH protocol or direct CSF measurements, please see published works[32,53,138], or additional information can be addressed via contact with the corresponding article of this manuscript.

- This paper does not report original code. All previously published algorithms are listed in the key resources table.

- Any additional information required to reanalyze the data reported in this paper is available from the lead contact upon request.

EXPERIMENTAL MODEL AND SUBJECT DETAILS

Rodent Model—Animal experiments were performed under a protocol approved by the Institutional Animal Care and Use Committee (IACUC) of Yale University and in accordance with the guidelines and regulations in the NIH Guide for the Care and Use of Laboratory Animals. Male and Female Wistar rats (Charles River, Wilmington, MA, USA) of wild type and $Stk39^{-/-}$ [77] and $Tlr4^{-/-}$ [57] genotypes, aged 8 weeks (200–350g) and bred in accordance with an IACUC-approved protocol at the Yale University School of Medicine, New Haven, CT were anesthetized (90 mg/kg body weight ketamine plus 7.5 mg/kg body weight xylazine, i.p.) and allowed to breathe room air spontaneously. Body temperature was maintained at 37 ± 1 °C (Harvard Apparatus, Holliston, MA) throughout the course of the experiments. This study randomly chose animals for either control or experimental conditions and the researchers were not blinded. Female rats were excluded from this study to avoid introducing sex as an additional variable. Animals were determined to be healthy by the veterinary staff, were immunocompetent, no involved in previous procedures (other than those directly related to this project and described below in the Methods Details section), were drug and test naïve (other than those directly related to this project and described below in the Methods Detials section), and were kept under standard, IACUC approved husbandry and housing conditions at Yale.

Porcine Model—All porcine studies were performed in collaboration with the Dardik laboratory at Yale University and in compliance with federal guidelines and protocols approved by the Yale University Institutional Animal Care and Use Committee. Yorkshire male pigs, with mean age of 3.4 months, were delivered to our facility 7-10 days prior to any procedures, kept under standard and IACUC approved husbandry and housing conditions at Yale, and were determined to be healthy after examination by veterinary staff. Animals had not undergone any previous procedures and were drug and test naïve.

METHOD DETAILS

Model of post-hemorrhagic hydrocephalus—IVH was modeled using our previously published methods[30], and detailed here. In an anesthetized animal, the hair on the dorsal side of the skull was initially shaved using clippers. A 2.5-cm incision was made in the proximal tail (beginning 2.5 cm below the rectum) using a scalpel (Bard-Parker, #10 Carbon Steel Surgical Blade) and the tail artery was then aseptically cannulated using a flexible catheter (PE-20) pre-loaded with heparinized saline. The rat was then mounted in a stereotactic apparatus (Stoelting Co., Wood Dale, IL), a 2.5-cm midline scalp incision was made using a new scalpel blade to expose the aponeurosis, and the skin was retracted using Barraquer retractors (Harvard Apparatus). The aponeurosis was then cut via a midline incision and carefully retracted using the same scalpel. The surface of the skull was cleaned using 0.9% Sodium Chloride (Hospira, Lake Forest, IL) and dried using 16 ply 4x4 sterile

gauze sponges (Covidien, Mansfield, MA). Any bleeding from the skull was burned using a cautery pen (Bovie, Clearwater, FL). After the skull was dry, a 1 mm burr hole was made using a high-speed drill over the right lateral ventricle (coordinates, x= −0.8, y= −1.7 mm from bregma) and the skull was subsequently cleaned and allowed to dry using the same method as indicated above. Approximately 150 μL of blood was then drawn from the tail artery catheter into a 1 mL syringe initially filled with 500 μL of heparinized saline and was subsequently discarded. An additional 50 μL of blood was then drawn into a new, sterile 1 mL syringe and immediately transferred into a 500 μL syringe (Hamilton, Reno, NV), which was then mounted to the stereotactic frame. Under stereotactic guidance, 50 μL of freshly collected autologous blood, free from anticoagulants, was infused into the right lateral ventricle (coordinates, x= −0.8, y= −1.7, z= −4.5 mm from bregma), over the course of 5 minutes, and the 26-gauge needle was held in place for an additional 20 minutes to prevent blood backflow from the the burr hole upon needle removal. The incisions were then sutured with a simple uninterrupted stich using 4-0 2.0 Metric DemeGUT absorbable surgical suture (DemeTECH, Miami Lakes, FL). Intraventricular sterile aCSF (Harvard Apparatus) infused in the same manner served as the IVH control condition.

Model of post-infectious hydrocephalus—As in the model of post-hemorrhagic hydrocephalus outlined above, an anesthetized rat with shaved dorsal skull was mounted into a stereotactic apparatus (Stoelting Co.), and a 1-inch midline scalp incision was made with a scalpel blade to expose the fascia on the dorsal side of the skull. The aponeurosis was then incised midline and carefully retracted with the same scalpel blade. The surface of the skull was then cleaned using 0.9% Sodium Chloride, dried with 16 ply 4x4 sterile gauze sponges, and any skull bleeding cauterized by cautery pen. A high-speed drill was used to make a 1 mm burr hole in the dry skull over the right lateral ventricle (coordinates, x= −0.8, y= −1.7 mm from bregma), and the skull subsequently cleaned and allowed to dry as above. After the skull was sufficiently dry, a brain infusion cannula with depth adjusted to 4.5 mm using 1 spacer (Alzet, Cupertino, CA; brain infusion and cannula kit, #2) was mounted with veterinary surgical cyanoacrylate adhesive (Covetrus, Dublin, OH) into the right lateral ventricle (x= −0.8, y= −1.7 relative to bregma). A small horizonal incision was then made just above the spinotrapezius muscle overlying the neck and upper back. An osmotic pump (Alzet, 1003D, rate: 1mL/hr), filled 12h earlier with lipopolysaccharide (LPS; Enzo, Serotype O55:B5) diluted in aCSF (10ng/mL) or *E. coli* (Lucigen) diluted in aCSF (see below), was then placed subcutaneously in the caudal portion of the dorsum and connected to the cannula attached to the skull using PE tubing provided in the Alzet brain infusion kit. The incisions were then sutured via a simple uninterrupted stich using 4-0 2.0 Metric DemeGUT absorbable surgical suture. Control animals were treated identically, but with aCSF loaded into the osmotic pump.

ICV-infusion of *E. coli*—Wild-type *E. coli* and ClearColi (*E. coli* lacking functional surface LPS; Lucigen BD21; https://www.nature.com/articles/nmeth.f.367.pdf?origin=ppub) were cultured originally on standard LB-agar plates. A single colony from each strain was used for inoculation in 10 mLs of standard LB broth and incubated overnight at 37 degrees Celsius. To get a specific number of cells per milliliter, 10 mLs of LB was then inoculated with 100 μl of the overnight culture and grown at 37 degrees Celsius for 3 hours to achieve

bacterial growth at log phase. The cells were harvested by centrifugation at 2000RPM at 4 degrees Celsius for 10 minutes. The pellet was collected and resuspended in 50ml of PBS. 1 μl of the 50ml was then added to 10ml of LB. 10 μl of the primary dilution was added to 300 μl of LB and plated on a 10cm LB-agar plate. The plates were incubated at 37 degrees Celsius overnight. The number of bacterial colonies were counted, and the colonies/ml determined. This was then used to determine the volume of the 50 mL stock bacteria to be used for brain infusion. The 50ml stock bacteria was stored in 1xPBS with 10% glycerol at −80 degrees Celsius. *E. coli* cells were diluted into sterile aCSF and delivered ICV via osmotic pump (Alzet 1003D, rate 1μl/hr) as detailed above for our model of PIH.

Measurement of CSF production rates—Rates of CSF production were measured using our published method[30,53], and as described here. Anesthetized rats were mounted in a stereotactic apparatus and a 1.3 mm burr hole was made over the left lateral ventricle (coordinates, x= −0.8, y= +1.7 relative to bregma). The mounted head was rotated on the ear-bars 90°, nose-down, and the suboccipital muscles were dissected to the cisterna magna to expose the atlanto-occipital ligament. The ligament was punctured, and a 23-gauge flexible catheter (PE-20) was advanced 5 mm through the foramen of Magendie to the 4th ventricle. Sterile, molecular grade mineral oil (100 μL; Sigma Aldrich, St. Louis, MO) was infused into the 4th ventricle to occlude the aqueduct of Sylvius, thereby creating a closed system of CSF circulation. With the rat in the same position, a glass capillary tube (cat # CV8010-300; borosilicate; OD, 1 mm; ID, 0.8 mm; length, 30 cm; VitroCom, Mountain Lakes, NJ) was advanced through the burr hole into the right lateral ventricle (4.5 mm beyond entry). The volume (V) of CSF that had formed at a given timepoint was calculated as: $V(mm^3) = \pi \cdot r^2 \cdot d$, where r is the radius of the capillary tube and d is the distance CSF traveled within the capillary. Pictures were taken every 5 min over the course of 30 min. The rate of CSF formation (μL/min) could be calculated from the slope of the volume–time relationship.

Ventricular volume analysis—Ventricular volume analysis was performed as we previously published[30], and as described here. Rats were transcardially perfused with 40 mL of ice-cold normal TBS (pH=7.60) followed by 40 mL of ice-cold 10% neutral buffered formalin (NBF; EMD Millipore Corporation). Brains were harvested and kept in 10% NBF overnight, then transferred to a 30% sucrose solution for cryoprotection. The brains were then removed, placed in Optimal Cutting Temperature Compound (OCT; Tissue-Tek, Sakura) for 1hr at room temperature and frozen in dry ice. The mounted brains were kept at −80°C until transfer to the cryostat, then left 1hr at −20°C. Brains were then serially sectioned in 25 μm sections). To prevent distortion from cryosectioning and slide mounting, we took high resolution pictures of serial coronal sections (200 μm apart, 14 levels) while the brain was mounted in the cryostat, using uniform parameters of camera positioning, magnification, and external lighting. Imaging software Gimp-2.10 was used to obtain a pixel count of the lateral ventricular and whole brain area of each section. A pixel to mm conversion factor was generated using the standard distance 22 mm sized block. Pixels were converted to area in mm2, summed over 14 levels and multiplied by the distance between levels (0.2 mm) to calculate ventricular and brain volume. The ventricular volume was divided by the brain volume to correct for varying brain size among animals.

ICV bumetanide delivery—As previously described[30,140], at the time of CSF collection prior to rotating the rat's head to a vertical orientation, a 28-gauge cannula from an Alzet brain infusion kit (#2; Durect) with a single spacer to adjust the depth to 4.5 mm, was stereotactically placed with a single spacer to adjust the depth to 4.5 mm into the burr hole over the left lateral ventricle (coordinates, x= −0.8, y= +1.7 relative to bregma) and secured to the skull with cyanoacrylate adhesive. The cannula was connected via a preloaded PE-20 catheter to a 1-ml syringe containing bumetanide (2.7 mM, pH 9; Sigma-Aldrich) diluted in aCSF (Harvard Apparatus). The syringe was loaded into a syringe infusion apparatus (Pump elite 11, Harvard Apparatus) and maintained at 37 °C. To determine the rate of CSF formation during intraventricular drug infusion, the 'actual infusion rate' of the drug (1.93 μl/min) was subtracted from the 'measured outflow rate' to obtain the operational 'calculated rate of CSF formation'. To assess the effect of a drug, the baseline rate of CSF formation was determined during spontaneous CSF formation (no drug infusion), and the calculated rate of formation was then determined after infusion of bumetanide.

Systemic rapamycin administration—Rapamycin (6mg/kg in normal saline, IP, Cayman) was administered IP 2-3hr prior to the start of IVH and LPS surgery. At 48h for IVH-treated rats and 72h for LPS-treated rats, rats were then either (i) euthanized and transcardially perfused with TBS (pH=7.60) and 10% NBF and processed for ventriculomegaly or immunohistochemistry analysis as described above, or (ii) anesthetized for surgery to allow measurement of the rate of CSF secretion as described above.

ICV injection of Evans Blue Dye—Based on our previous methods to determine communication between the cerebral ventricles[53], Evans Blue Dye (Sigma Aldrich; 0.5% in sterile aCSF) was loaded into a 1mL syringe (BD Syringe, Franklin Lakes, NJ) and connected to a cannula (Alzet; brain infusion and cannula kit, #2) using PE tubing. Anesthetized rats were mounted in a stereotactic apparatus and a 1.0 mm burr hole was made over the right lateral ventricle (coordinates, x= −0.8, y= −1.7 relative to bregma). The cannula was placed into the right lateral ventricle and dye was infused at a nominal rate of 2μL/min for 5 minutes with a syringe pump (Harvard Apparatus; Elite 11). Following infusion, the cannula remained in the ventricle for 30 minutes to prevent back flow and assure adequate circulation of the dye within the CSF spaces. Animals were then transcardially perfused with ice cold TBS (pH = 7.60), brains were harvested and immediately cut sagittally along the interhemispheric line. Images were taken to show the level of patency of the cerebral aqueduct.

CSF cytokine collection—48h after surgery for the PHH model or 72h following surgery for the PIH model, anesthetized rats were mounted in a stereotactic apparatus. The rat's head was rotated on the ear-bars 90°, nose-down, and the suboccipital muscles were dissected to the cisterna magna to expose the atlanto-occipital ligament. The ligament was punctured using a 27G PrecisionGlide needle (BD, Franklin Lakes, NJ) attached to a 1mL syringe (BD, Franklin Lakes, NJ) and inserted into the cisterna magna. CSF (~100mL) was slowly withdrawn into a syringe and immediately transferred to a 1.5 mL Eppendorf tube on dry ice. Rats were immediately euthanized following CSF collection. Samples were stored at

−80°C until shipment on dry ice to Eve Technologies (Calgary, CA) for analysis using their Rat Cytokine Array / Chemokine Array 27 Plex (RD27).

Rodent choroid plexus epithelium harvesting—Immediately following transcardial perfusion with ice cold TBS (pH = 7.60), the brain was isolated and placed in an ice-cold saline bath. Brains were cut sagittally along the interhemispheric line to expose the lateral ventricles, and choroid plexuses were rapidly but carefully dissected from both lateral ventricles using sharp forceps under magnification. Each brain yielded ~3 mg of choroid plexus tissue total, which was collected into a 1.5 mL tube, snap frozen in liquid nitrogen, and stored at −80°C until use.

Immunohistochemistry—Rats were transcardially perfused with ice-cold TBS followed by 10% NBF. Brains were dissected, kept in formalin overnight and dehydrated before paraffin embedding. 5-micron paraffin sections were rehydrated (briefly, slides were incubated in Xylene x10 min (x2), 100% ethanol x5 min (x2), then 95% ethanol x5 min (x2), then 70% ethanol (x1), then washed briefly in diH$_2$O) prior to antigen-retrieval at 95°C for 40 min using a citrate-based buffer (Retrieve-all system 1, Biolegend). After three TBST washes, the sections were incubated in blocking solution (5% donkey serum solution / TBST) for 1h at room temperature. The primary antibodies (diluted 1:200 in blocking solution) were incubated overnight at 4°C. After three TBST washes, secondary antibodies diluted 1:500 (Alexa Fluor 488, Alexa Fluor 555, Alexa Fluor 647; Invitrogen, Molecular probes) and DAPI (5ug/ml, Biolegend) was added to the sections and incubated for 1 hour at room temperature and washed in TBST before mounting in Prolong Gold Antifade reagent (Invitrogen) and analysis by epifluorescence microscopy (Nikon Eclipse 90i, Nikon Instruments). The following antibodies were used: AQP1 (Abcam, Rabbit recombinant monocolonal, ab168387), ATP1A1 (Alomone, rabbit polyclonal, ANP-001), CD68 (CST, rabbit monoclonal, 97778), CLIC6 (Santa Cruz, mouse monoclonal, 365303), ED1/CD68 (Millipore, mouse monoclonal, MAB1435), IBA1 (Thermo, goat polyclonal, PA5-18039), KCNJ13 (Santa Cruz, mouse monoclonal 398810), Ki67 (CST, rabbit monoclonal 9129), pNKCC1 (Millipore, rabbit polyclonal, ABS 1004), pSPAK (Millipore, rabbit polyclonal, 07-2273), RELT (Novus, rabbit polyclonal, NBP2-56851), NKCC1 (CST, rabbit monoclonal, 85403S). Colocalization analysis was performed using the Fiji Coloc 2 plugin[141].

Tissue dissociation and flow cytometry—Animals were anesthetized with Ketamine/ Xylazine and transcardially perfused with ice cold TBS before brain removal. Choroid plexi from bilateral lateral ventricles were microdissected in ice cold HBSS and digested at 37°C for 20 min with Collagenases-I (10 U/mL) and -IV (400 U/mL) and DNaseI (30 U/mL) (this protocol was adapted from Van Hove et al[58]). The cell suspension was blocked with CD16-CD32 antibodies and stained 30 min at 4°C with anti-rat CD45-PE/cy7, CD3-647 or corresponding isotype antibodies (Biolegend) and DAPI- co-stained to monitor cell viability. Cells were subsequently washed in FACS staining buffer (0.5% BSA, 2mM EDTAin PBS without Calcium/Magnesium) and centrifuged at 350 rcf for 5 minutes. For FACS, cells were resuspended in 300ul of FACS buffer and sorted on a BD ARIA instrument, with gating and analysis by FlowJo software.

Antibodies for western blots—Primary antibodies used were: anti-WNK1 (University of Dundee, S079B), anti-SPAK (University of Dundee, S365D), anti-NKCC1 total antibody (University of Dundee, S022D), anti-Na(+)/K(+) ATPase alpha-1 (ATP1A1) antibody (DSHB, a5), anti-beta Actin antibody (Abcam, ab8227). Horseradish peroxidase-coupled (HRP) secondary antibodies used for immunoblotting were from Pierce. IgG used in control immunoprecipitation experiments was affinity-purified from pre-immune serum using Protein G-Sepharose.

Buffers for Western blots—Buffer A contained 50 mM Tris/HCl, pH 7.5 and 0.1 mM EGTA. Lysis buffer was 50 mM Tris/HCl, pH 7.5, 1 mM EGTA, 1 mM EDTA, 50 mM sodium fluoride, 5 mM sodium pyrophosphate, 1 mM sodium orthovanadate, 1% (w/v) NP40, 0.27 M sucrose, 0.1% (v/v) 2-mercaptoethanol, and protease inhibitors (complete protease inhibitor cocktail tablets, Roche, 1 tablet per 50 mL). TBS-Tween buffer (TTBS) was Tris/HCl, pH 7.5, 0.15 M NaCl and 0.2% (v/v) Tween-20. SDS sample buffer was 1X NuPAGE™ LDS Sample Buffer (NP0007, Invitrogen™), containing 1% (v/v) 2-mercaptoethanol. Protein concentrations were determined following centrifugation of the lysate at 16,000 x g at 4°C for 20 minutes using the using a Pierce™ Coomassie (Bradford) Protein Assay Kit (23200, Thermo Scientific) with bovine serum albumin as the standard.

Immunoblot and immunoprecipitation analyses—Rat choroid plexus lysates were subjected to immunoblot and immunoprecipitation as previously described[30,142], and is detailed here. Rat choroid plexus lysates (20 μg) were boiled at 75°C in sample buffer for 10 minutes, resolved by 7.5% sodium dodecyl sulfate polyacrylamide-gel electrophoresis and electrotransferred onto a polyvinylidene difluoride membrane. Membranes were incubated for 30 min with TBST (Tris-buffered saline, 0.05% Tween-20) containing 5% (w/v) skim milk. Blots were then washed three times with TBST and incubated for 1 h at room temperature with secondary HRP-conjugated antibodies diluted 5000-fold in 5% (w/v) skim milk in TBST. After repeating the washing steps, signals were detected with enhanced chemiluminescence reagent. Immunoblots were developed using ChemiDoc™ Imaging Systems (Bio-Rad, Feldkir). Figures were generated using Photoshop/Illustrator (Adobe).

SPAK was immunoprecipitated from rat choroid plexus lysates clarified by centrifugation at 16,000 x g at 4°C for 20 minutes, using SPAK antibody coupled to protein G–Sepharose[30,142] at a ratio of 1 mg antibody per 1 mL beads. Clarified cell lysate (2 mg) was incubated 2 h at 4°C with 15 μg of antibody conjugated to 15 μL of protein-G–Sepharose with gentle agitation. Beads were washed three times with 1 mL lysis buffer containing 0.15 M NaCl and twice with 1 mL buffer A. Bound proteins were eluted with 1X LDS sample buffer.

qPCR analysis—Microdissected tissues were snap frozen and stored at −80°C until total RNA was extracted using RNeasy Micro plus kit (Qiagen, 74034) and reverse transcribed (Biorad, 170-8890). Gene expression analysis was determined by quantitative reverse-transcription PCR (Bimake, B21202) using a CFX96 PCR machine (Bio-Rad). The qPCR primer sequences are provided in Table S5. The data were expressed using the comparative threshold cycle (CT) method (GOI, Gene Of Interest vs. Gapdh), and the

mRNA ratios were given by 2^{-CT} compared to Housekeeping genes. Gapdh expression was also compared to another Housekeeping Gene (Hprt1), as an additional control.

Bulk RNAseq—Full length high quality total cell RNA isolated by Qiagen RNAeasy micro kit (Quigen, https://www.qiagen.com/us/shop/pcr/rneasy-micro-kit/). ChP cells were homogenized in 350ul RLT buffer with beta-mercaptoethanol in Tissuelyzer for 10 mins and proceed according to the instructions in RNAeasy Micro RNA kit and RNAs was eluted in 18ul dH2O. 16ul of elutant was recovered and 1.2ul was used for the QC. Libraries were run on an Illumina HiSeq 2500 at the Yale Center for Genome Analysis. Expression level for each gene was estimated using Python program HTSeq[143]. Specifically, htseq-count function of HTSeq accumulated the number of aligned reads that falls under the exons of the gene. The R/Bioconductor package "DESeq2" was used to identify differentially expressed genes between cell populations derived from control, IVH-treated and LPS-treated rats[144]. Genes with a log2-fold change expression greater than 3 and a q-value less than 0.01 were considered significant. The R ComplexHeatmap package was used to visualize the heatmap expression of highly variable genes[145]. Volcano plots were generated using the R package EnhancedVolcano.

scRNAseq sample preparation—Animals were anesthetized with Ketamine/Xylazine and transcardially perfused with ice cold TBS before brain removal. Choroid plexi from bilateral lateral ventricles were microdissected in ice cold HBSS with 30uM Actinomycin D (ActD, Sigma, cat#A1410) and digested at 37°C for 20 min with Collagenases-I and -IV (10 U/mL, 400 U/mL final, Worthington, Cat# LS004194, and LS004184) and DNase I (30 U/mL, Roche, cat# 04716728001) and ActD (3uM) (this protocol was adapted from Van Hove et al[58]). For Flow sorting, the cell suspension was blocked with CD16-CD32 antibodies (1:100, biolegend, cat#101302) and stained 30 min at 4°C with anti-rat CD45-PE/cy7 (1:100, biolegend, cat#202207) to and DAPI (50ug/mL). Cells were subsequently washed in FACS staining buffer (0.5% BSA, 2mM EDTA in PBS without Calcium/Magnesium) and centrifuged at 350 rcf for 5 minutes. Cells were resuspended in 300ul of FACS buffer and sorted by CD45 positivity on a BD ARIA instrument. CD45 positive and CD45 negative cells were collected in 0.4% BSA/PBS and 3uM ActD and sent for 10X 3prime library preparation and sequencing at Yale Center for Genome Analysis.

Anesthesia and CM catheter placement—The rats were anesthetized with ketamine-xylazine (90 mg/kg bodyweight ketamine plus 7.5 mg/kg bodyweight xylazine, i.p.) and after loss righting reflex they breathed an Air:O$_2$ mix (1:1) spontaneously via a nose cone. Anesthesia was maintained with KX administered every 30 min via an IP catheter. When surgical plane anesthesia was assured by toe pinch before placing the rats in a stereotaxic frame. The dura above the cisterna magna (CM) was exposed and a small 5-mm copper tube (0.32 mm o.d., Nippon Tockushukan, MFG. CO., LTD, Tokyo, Japan) attached to a PE 10 microcatheter was positioned into the CSF compartment and secured in place using cyanoacrylate glue. After surgery, the rats were transferred to the MRI animal bed equipped with a heating waterbed and nose cone.

Magnetic resonance imaging (MRI)—All MRI acquisitions were performed on a Bruker 9.4T/16 magnet (Bruker BioSpin, Billerica MA) interfaced to an Avance III console controlled by Paravision 6.0 software. We used a 30-mm ID planar surface radiofrequency (RF) coil (Bruker BioSpin, Billerica, MA, USA) which was placed under the head of the rats for RF signal reception and a custom-made volume transmit RF coil designed with an internal diameter of 50 mm was used as RF signal transmitter. While in the MRI instrument, the rats were in supine position and breathed an Air:O_2 mix (1:1) spontaneously via a nose cone. Heart rate (HR) via oxygen saturation monitoring, respiratory rate and body temperature were continuously monitored (SA Instruments, Stony Brook, NY, USA). The body temperature was kept within ~ 37.0°C using a heated waterbed and oxygen saturation was kept 97% during the MRI experiments. **Brain morphometry**: A single flip angle spoiled gradient echo (SPGR) sequence was used to acquire 3D proton density weighted (PDW) MRIs: (repetition time (TR) = 50ms, echo time (TE) = 4ms, flip angle (FA) = 7°, Average = 2, field of view (FOV) = 30x30x15mm, spatial resolution = 0.234x0.234x0.234mm, scan time ~ 14min. **Dynamic contrast enhanced MRI**: We acquired pre-contrast (baseline) T1-weighted images and post-contrast T1-weighted imaging of the whole brain. The 3D T1 weighted scans were acquired using a single flip angle spoiled gradient echo (SPGR) sequence: TR=15ms, TE=4ms, FA=15°, Average = 2, FOV = 32x30x30mm, the spatial resolution= 0.302x0.300x0.300mm, acquisition time/scan = 5mins). After three baseline T1-weighted scans, 30 μL of 1:10 gadoteric acid (Gd-DOTA, DOTAREM, Guerbert LLC, Carol Stream IL) diluted in sterile water was infused at a rate of 1.5 μL/min into CSF through the CM catheter using an infusion pump for a total of 20 min. Post-contrast T1-weighted scans continued for a total 160 min.

Porcine choroid plexus epithelium harvesting—All porcine studies were performed in collaboration with the Dardik laboratory at Yale University and in compliance with federal guidelines and protocols approved by the Yale University Institutional Animal Care and Use Committee. Male Yorkshire pigs of ~48 kg and aged 3.4 months were euthanized via lethal injection of Euthasol (0.22 ml/kg)[54]. Euthanized pigs were placed prone on the operating table for brain dissection. A semicircular scalp incision was made around the vertex of the cranium, the skin was retracted, and the periosteum removed. Using an oscillating bone saw (Dremel Multi-max; Illinois, USA) a frontal craniectomy was performed to expose the underlying dura and cerebral hemispheres. The dura was excised at the midline to gain access to the superior sagittal sinus. The cerebral hemispheres were separated using surgical forceps and the lateral and third ventricles were exposed. The choroid plexus, identified as a highly vascular intraventricular structure, was carefully removed via forceps and placed into sterile saline on ice for molecular analysis.

Mass-spectrometry (MS) proteomics—Frozen pellets of ChP cells were lysed by sonication in RIPA buffer plus 1× PhosSTOP phosphatase inhibitor (Roche) and 1× cOmplete protease inhibitor cocktail (Roche). Protein (200 μg) for each sample underwent reduction, alkylation, and chloroform-methanol precipitation. Samples were resuspended in 100 mM TEAB (pH 8.5) and digested with trypsin (Promega, 1:50 w/w) overnight at 37°C. Digested samples were acidified and desalted on a C18 Macro Spin Column (The Nest Group). Peptides were eluted in 80% acetonitrile/0.1% trifluoroacetic acid (TFA), then dried

by a SpeedVac. The dried peptide pellet from each sample was then TMT labeled according to manufacturer's protocol (Thermo Fisher Scientific) using a TMT10Plex Isobaric Labeling Reagent Kit (Cat#:90110). A label efficiency test was performed on 1/50th of each sample prior to equally mixing the 10 channels, then samples were dried prior to fractionation. Pooled TMT labeled peptides were then dissolved in buffer A and injected onto a Waters ACQUITY UPLC (BEH) C18 column (Waters XBridge BEH130 C18 3.5 μm 4.6 × 250 mm) at a flow rate of 0.4 mL/min. An orthogonal high pH reverse phase separation was carried out using a Waters H-class UPLC system with Buffers (A:95% water/5% acetonitrile (ACN) with 10 mM ammonium acetate, pH 10; B: 5% water/95% acetonitrile (ACN) with 10 mM ammonium acetate, pH 10) were used to separate the peptides with a 60 min gradient 15% – 55% with buffer B. Total 60 fractions were collected. The fractions were then pooled into 8 fractions, dried and reconstituted in 0.1% formic acid.

Mass spectrometry data were obtained on an Orbitrap Fusion Tribrid Mass Spectrometer (ThermoFisher Scientific, San Jose, CA, USA) coupled to a nanoACQUITY UPLC system (Waters Corporation, Milford, MA, USA) in the Keck MS & Proteomics Resource at Yale University as described in Lee et. al[146], and detailed here. Individual pooled fractions were loaded into a trapping column (nanoACQUITY UPLC Symmetry C18 Trap column, 180 μm × 20 mm and separated with a C18 column (nanoACQUITY column Peptide BEH C18, 75 μm × 250 mm) at a flow rate of 5 μL/min. Peptides were eluted with a gradient from 6% to 20% mobile phase B over 120 min and then to 40% mobile phase B for another 45 min at a flow rate of 300 nL/min at a flowrate of 300 nL/min with buffers (A: 0.1% formic acid in water and B: 0.1% formic acid in acetonitrile). The data were acquired with data-dependent mode with multinotch synchronous precursor selection (SPS)-MS3 scanning for TMT tags as described previously[147]. The ions above with an intensity threshold of 5000 was selected for collision-induced dissociation (CID)-MS fragmentation. The top 10 fragment ions for each peptide MS2 were notched out and co-fragmented with higher-energy collision dissociation (HCD) to produce MS3 scans and were analyzed in the Orbitrap at a resolution of 60,000.

The proteomics raw data files were processed and quantified by MaxQuant (https://maxquant.net/maxquant/) version 1.6.1.0 with Andromeda search engine using the Rat UniProt FASTA database (http://coxdocs.org/doku.php?id=maxquant:andromeda:start). Default value of parameters were used in Maxquant unless explicitly stated. Briefly, false-discovery rate (FDR) was set 1% for proteins and peptides respectively and match between runs was enabled with a default time window of 0.7 min. Search results (TMT reporter ion intensities) were exported as text files. The differentially expressed proteins were identified using the Perseus framework (https://maxquant.net/perseus/). Proteins with a log2-fold change expression greater than 1 and a q-value less than 0.05 were considered significant. The R ComplexHeatmap package was used to visualize the heatmap expression of highly variable genes[145].

SPAK Immunoprecipitation for LC-MS/MS—ChP cells were lysed in a lysis buffer containing protease and phosphatase inhibitor by incubating 10 min on ice and then centrifuged at 18.000 g for 5 min at 4°C. Supernatants containing the proteins were first precleared with Protein G beads for 30 min at 4°C and then were split in half and transferred

into two clean 1.5 mL Eppendorf tubes. One half of the supernatant was incubated with Protein G beads only (IgG) as control for non-specific binding; the other half of the supernatant was incubated with Protein G beads + anti-SPAK 1°Ab. Incubation with gentle agitation was conducted at 4°C for overnight. Supernatant was removed and beads were washed 4 times with RIPA containing 150mM NaCl. Bound proteins were then eluted twice with 2M urea (for in-solution trypsin digestion) or SDS sample buffer for 5 minutes (In-gel trypsin digestion). The elutions of SDS samples buffer were then loaded onto a mini SDS PAGE gel (4-12%, Bio-Rad Laboratories, Hercules, CA). Gel bands/plugs were excised and processed for LCMS/MS analysis[148]. Gel bands/plugs were first cut into small pieces and subjected to the following washes with agitation: 50% (v/v) acetonitrile (5 min), 50% (v/v) acetonitrile/10 mM NH_4HCO_3 (30 min). Gel pieces were dried with a SpeedVac, resuspended in 30 μL of 10 mM NH_4HCO_3/0.2 μg digestion grade trypsin (Promega), and incubated for 16 h at 37 °C. Peptides were then acidified with 0.1% (v/v) trifluoroacetic acid (TFA) prior to LC MS/MS analysis on an Orbitrap Fusion mass spectrometer coupled to a nanoACQUITY UPLC[149] located within the Keck MS & Proteomics Resource at Yale.

QUANTIFICATION AND STATISTICAL ANALYSIS

Data analysis—Statistical analysis of CSF secretion, CSF cytokine analysis, ventriculomegaly, and IHC quantification used Prism (GraphPad, San Diego, CA) for one-way ANOVA analysis with Tukey's multiple comparisons, unpaired t-test, or paired t-test. Transcriptomic and proteomic data was analyzed using RStudio (RStudio Inc., Boston, MA). Non-parametric Wilcoxon rank sum test was used to determine statistically significant gene markers in scRNAseq datasets. Numerical data in text and figures are presented as mean ± standard error of the mean (SE). Rates (μL/min) were calculated as the slope of the volume-time relationship, based on data collected over 20 min or more. Rates were determined for individual animals and averaged across individuals. Sample size calculations were based on two previous studies that used the same model of IVH [30] and method for measuring rates of CSF production [30,53]. The statistical details of each experiment can be found in the figures and corresponding figure legends (including the specific statistical test used, value of n and what each n represents, and the dispersion and precision measures used), except for the scRNAseq datasets. Details for the specific analysis used for the scRNAseq datasets are detailed in the Method Details of the STAR Methods section. Any additional information can be addressed via contact with the corresponding article of this manuscript.

snRNA-seq rat ChP data analysis—As described previously[2], the preprocessing and clustering analysis for snRNA mouse choroid plexus cell dataset was completed using Seurat[150]. For each nucleus, the number of genes for which there was at least one mapped read, was quantified, and then all nuclei with fewer than 500 detected genes were excluded. Furthermore, all nuclei with more than 10% of total UMI's mapped to mitochondrial genes were excluded. Genes detected in fewer than 10 nuclei were excluded. Expression values $E_{i,j}$ for gene i in nucleus j were calculated by dividing UMI counts for gene i by the sum of the UMI counts in nucleus j, to normalize for differences in coverage, and then multiplying by 10,000 to create TPM-like values (TP10K), and finally computing $\log_2(TP10K + 1)$.

Selection of variable genes was performed by fitting a logistic regression model to the cellular detection fraction (often referred to as α), using the total number of UMIs per cell/nucleus as a predictor, as in Montoro et al., 2018[151]. Outliers from this curve are genes expressed in a lower fraction of cells/nuclei than would be expected, given the total number of UMIs mapping to that gene; that is, likely cell-type or state-specific genes. A threshold of deviance between < -0.15 and < -0.3 was used.

The expression matrix was restricted to the subsets of variable genes and high-quality cells/nuclei noted above, and then centered and scaled values before inputting them into principal component analysis (PCA), implemented using 'RunPCA' in Seurat which runs the irlba function. For the snRNA-seq data, which included mixed sexes, Y chromosome and X-inactivation genes (Xist, Tsix) were removed from the variable genes prior to running PCA. The cell embeddings were either the singular vectors themselves or the singular vectors multiplied with the singular values depending on the cell type. After PCA, significant principal components were identified using the elbow-method, when looking at the distribution of singular values. Scores from only those significant principal components were used as the input to further analysis. To embed cells in a graph structure, first a KNN graph was constructed based on the euclidean distance in PCA space, and the edge weights were refined between any two cells based on the shared overlap in their local neighborhoods (Jaccard similarity). This step was performed using the FindNeighbors (reduction='pca', dims=1:50) command by taking the first 50 principal components as input. To cluster the cells in an unsupervised fashion, the Louvain algorithm (default) was applied to iteratively group cells together, with the goal of optimizing the standard modularity function. The FindClusters(resolution=0.5) function was implemented for this procedure. For visualization purposes, the dimensionality of the datasets was further reduced to 2D embeddings using UMAP on the significant PCs via RunUMAP() functions of the Seurat package in R[152]. Non-parameteric Wilcoxon rank sum test was used to identify differentially expressed markers across all clusters by running FindAllMarkers(dataset, only.pos = TRUE, min.pct = 0.25, logfc.threshold = 0.25). VlnPlot(), which shows expression probability distributions across clusters, and FeaturePlot(), which visualizes feature expression on a UMAP plot) were used to visualize key genes differentially expressed for individual clusters. Adult epithelial cells were isolated and further sub-clustered in an unsupervised fashion using the Louvain algorithm.

Nucleus doublets were identified using the R package DoubletFinder (version DoubletFinder_2.0.2[153]. Briefly, artificial doublets are generated from the data, and for each real data point the fraction of artificial doublets of the nearest neighbors in a latent space is computed. If this fraction is above a certain cutoff, the data point is a doublet. Doublets were calculated for each sample separately after initial data filtering by genes detected and mitochondrial gene expression as per instructions. For each sample, an optimal pK (defines the PC neighborhood size) was chosen by computing a parameter sweep (paramSweep_v3 function), and a pK was chosen that maximized the BCmvn (mean-variance-normalized bimodality coefficient). Doublets were then calculated using the function doubletFinder_v3() with parameters; PCs = 1:30, pN = 0.25, nEXP = 15% of cells in the sample, and removed from downstream analysis.

PIH and PHH rat ChP scRNAseq datasets—The preprocessing and clustering analysis for scRNA rat choroid plexus CD45$^+$ and CD45$^-$ cell datasets for was completed using Seurat [150]. Cells with low numbers of genes (200), low numbers of UMIs (500) or high numbers of UMIs (>10000) and mitochondrial gene percentage greater than 10% were removed. The normalization and initial feature selection for each of the six datasets (control, IVH-treated, LPS-treated conditions for CD45$^+$ and CD45$^-$ cells) were completed individually. The filtered matrices were normalized using 'LogNormalize' methods in Seurat using a size factor of 10,000 molecules for each cell. 2,000 most variable genes were identified by variance stabilizing transformation for each dataset by implementing the FindVariableFeatures function in Seurat v4 (selection.method = "vst"). The experimental conditions were integrated using Seurat's integration pipeline for CD45$^+$ and CD45$^-$ cell datasets. For integration, 2,000 shared highly variable genes were identified using Seurat's 'SelectIntegrationFeatures()' function. Integration anchors were identified based on these genes using canonical correlation analysis using the 'FindIntegrationAnchors()' function. The data were then integrated using 'IntegrateData()' and scaled again using 'ScaleData()'. Overall, integrated CD45$^+$ dataset consisted of 1427 control, 3331 IVH-treated and 5529 LPS-treated cells whereas integrated CD45$^-$ dataset consisted of 2036 control, 718 IVH-treated and 1603 LPS-treated cells.

Principal component analysis (PCA) and uniform manifold approximation and projection (UMAP) dimension reduction with 50 principal components were performed. A KNN graph was constructed based on the euclidean distance in PCA space to embed cells in a graph structure, and the edge weights were refined between any two cells based on the shared overlap in their local neighborhoods (Jaccard similarity). This step was performed using the FindNeighbors (reduction='pca', dims=1:50) command by taking the first 50 principal components as input. To cluster the cells in an unsupervised fashion, the Louvain algorithm (default) was applied to iteratively group cells together, with the goal of optimizing the standard modularity function. The FindClusters(resolution=0.4) function was implemented for this procedure. For visualization purposes, the dimensionality of the datasets was further reduced to 2D embeddings using UMAP on the significant PCs via RunUMAP() functions of the Seurat package in R[152]. Non-parameteric Wilcoxon rank sum test was used to identify differentially expressed markers across all clusters by running FindAllMarkers(dataset, only.pos = TRUE, min.pct = 0.25, logfc.threshold = 0.25). Further sub-clustering of certain cell populations imcluding myeloid cells, T-cells, epithelial cells were conducted in an unsupervised fashion using the Louvain algorithm. The R ComplexHeatmap package was used to visualize the heatmap expression of highly variable genes[145]. VlnPlot, FeaturePlot and DotPlot functions were used to visualize the gene expression profiles across clusters and conditions

To infer cell–cell interactions based on the expression of known ligand–receptor pairs in different cell types, CellChat was applied to our experimental conditions after merging CD45$^+$ and CD45$^-$ for each condition. The official workflow and databases were implemented. Briefly, the normalized counts were loaded into CellChat after which the preprocessing functions identifyOverExpressedGenes, identifyOverExpressedInteractions and projectData with standard parameters set were applied to our datasets.

The main analyses were conducted using the functions computeCommunProb, computeCommunProbPathway and aggregateNet with fixed randomization seeds.

ScRNA-seq mouse ChP immune cell data analysis—As described previously [2], the preprocessing and clustering analysis for ScRNA mouse choroid plexus immune cell dataset was completed using Seurat [150]. Outlier cells were first identified based on three metrics (library size, number of expressed genes and mitochondrial proportion); cells were tagged as outliers when they were four median absolute deviations distant from the median value of each metric across all cells. Secondly, a principal component analysis plot was generated based on the following metrics:'pct_counts_in_top_100_features','total_features_by_counts', 'pct_counts_feature_control','total_featur es_by_counts_feature_control', 'log10_total_counts_endogenous' and 'log10_total_counts_feature_control'. Outlier cells in this principal component analysis plot were identified using the R package mvoutlier. Low-abundance genes were removed using the 'calcAverage' function and the proposed workflow. The raw counts were normalized and log2 transformed by first calculating 'size factors' that represented the extent to which counts should be scaled in each library. Highly variable genes were detected using the proposed workflow of the scran R package and by applying false discovery rate 0.05 and var.out$bio 0.01 as cutoffs. Highly variable genes were subsequently used for unsupervised dimensionality reduction techniques and principal component analysis.

To embed cells in a graph structure, first a KNN graph was constructed based on the euclidean distance in PCA space, and the edge weights were refined between any two cells based on the shared overlap in their local neighborhoods (Jaccard similarity). This step was performed using the FindNeighbors (reduction='pca', dims=1:50) command by taking the first 50 principal components as input. To cluster the cells in an unsupervised fashion, the Louvain algorithm (default) was applied to iteratively group cells together, with the goal of optimizing the standard modularity function. The FindClusters (resolution=0.5) function was implemented for this procedure. For visualization purposes, the dimensionality of the datasets was further reduced to 2D embeddings using UMAP on the significant PCs via RunUMAP() functions of the Seurat package in R[152]. Non-parameteric Wilcoxon rank sum test was used to identify differentially expressed markers across all clusters by running FindAllMarkers (dataset, only.pos = TRUE, min.pct = 0.25, logfc.threshold = 0.25). VlnPlot(), which shows expression probability distributions across clusters, and FeaturePlot(), which visualizes feature expression on a UMAP plot) were used to visualize key genes differentially expressed for individual clusters.

Induction of immediate early genes (IEGs) was observed in some of the Choroid Plexus cells in which two clearly separated macrophage clusters differed only in expression of IEGs and heat shock proteins were observed. These differentially expressed genes closely resembled those identified in a subset of muscle satellite cells and shown to be dissociation-induced genes. Single-cell isolation using either a standard or ActD modified protocol was compared to confirm that the IEGs induced in our clusters were also dissociation-induced. This allowed us to identify 224 genes that were upregulated in standard versus ActD samples in Choroid Plexus Border Associated Macrophages, comprising the dissociation-

induced gene list. To correct for dissociation-induced gene expression, which may mask biologically relevant results, this gene list was used to detect cells that were 'dissociation-affected' by plotting expression of all these genes over all cells. The corresponding histogram revealed a clear cutoff that split the cells between 'dissociation-affected' and unaffected cells. This information was added to the metadata attribute of the Seurat object, and this unwanted source of variation was subsequently removed using the 'Regress out' function of the Seurat R package.

Gene co-expression network creation—The gene co-expression modules for the preprocessed and clustered choroid plexus dataset were constructed by using Monocle3's differential expression analysis pipeline[154]. Monocle3's graph_test (neighbor_graph="knn") function was used to identify genes that vary between groups of cells in UMAP space. This function employs a statistic from spatial autocorrelation analysis called Moran's I, which Cao et al. showed to be effective in finding genes that vary in single-cell RNA-seq datasets[154]. Genes with FDR-adjusted p-values of less than 0.05 were used to construct gene co-expression networks via UMAP and community analyses. 21 gene modules were created using this pipeline.

Hypergeometric enrichment test analysis—Module gene lists were obtained via Monocle3 as described above. Hypergeometric enrichment analysis was conducted using the R package hypeR[155]. Syndromic and non-syndromic gene lists for both high confidence and probable genes were used to find modules enriched with Craniosynostosis-related genes. Modules with FDR adjusted p-values less than 0.05 were considered significant.

Cluster abundance analysis—In order to test the difference in cell counts for IVH-treated and LPS-treated ChP compared to control, we used beta-binomial generalized linear model in package aod::betabin for both $CD45^+$ and $CD45^-$ clustering. In our generalized linear model, we set the count of the cell type of interest and the total count of cells of each experimental condition to be the response variable and the experimental condition of the cells to be the independent variable. We tested for Pearson's correlation between the frequency of each cell cluster. We adjusted the p value threshold using Bonferroni correction ($0.05/32 = 0.00156$ for $CD45^+$ dataset and $0.05/20 = 0.0025$ for $CD45^-$ dataset).

Gene Ontology enrichment analysis—The gene and protein lists for differentially expressed genes and proteins for IVH and LPS conditions from the RNAseq and proteomics experiments, as well as the modules significantly enriched with these genes/proteins, were further studied for gene ontology, pathway and upstream transcription factor enrichment using the Enrichr R package[156]. The Enrichr contains a diverse and up-to-date collection of over 100 gene set libraries available for analysis and download. The databases for these analyses include gene ontologies (biological processes, cellular components, and molecular functions), biological pathways (Wiki pathways Human and Mouse) and upstream transcription factors (TRANSFAC and JASPAR). Adjusted p-value of less than 0.05 was considered significant and combined Z-score was used for ranking.

MRI data analysis—Morphometry of CSF and brain parenchyma (grey matter + white matter) volumes for each rat was performed as previously described (ref). Briefly, The 3D

PDW images were corrected for intensity inhomogeneity using the N4 bias field correction algorithm[157], and then segmented into grey matter (GM), white matter (WM) and CSF brain compartments to calculate their brain parenchymal (GM+WM) and CSF volumes. All the spatial segmentations were performed on SPM12 (http://www.fil.ion.ucl.ac.uk/spm) software package platform, using our previously custom-made tissue probability maps[158]. The tissue probability maps generated by segmentation of the individual rat brains were thresholded at 0.5, yielding GM, WM, and CSF binary masks in native space. Spatially normalized average CSF compartment volume maps of the sham controls (N=5) and LPS treated (N=6) rats were subsequently created. In addition to SPM analysis, for each rat manual segmentation of the lateral ventricle volume was performed on the PWD and T1-weighted baseline MRIs using PMOD (PMOD, version 3.908, PMOD Technologies LLC, Zürich, Switzerland). Analysis of DCE-MRI data included correction for head motion, followed by intensity normalization, smoothing, and then voxel-wise percent signal change to baseline was calculated using SPM12 (https://www.fil.ion.ucl.ac.uk/spm/)[159]. The 'percent signal change from baseline images' were then used for optimal mass transport (rOMT) analysis[160]. From each rat's whole brain DCE-MRI data series the rOMT analysis produced whole brain binary pathlines endowed with solute speed (representing the local speed and spatial distribution of the pathline networks) from which glymphatic flux and mean tissue solute speed was derived.[47]

Supplementary Material

Refer to Web version on PubMed Central for supplementary material.

ACKNOWLEDGMENTS

Inclusion and Diversity:

We support the inclusive, diverse, and equitable conduct of research.

References

1. Cui J, Xu H, and Lehtinen MK (2021). Macrophages on the margin: choroid plexus immune responses. Trends Neurosci 44, 864–875. 10.1016/j.tins.2021.07.002. [PubMed: 34312005]

2. Dani N, Herbst RH, McCabe C, Green GS, Kaiser K, Head JP, Cui J, Shipley FB, Jang A, Dionne D, et al. (2021). A cellular and spatial map of the choroid plexus across brain ventricles and ages. Cell 184, 3056–3074 e3021. 10.1016/j.cell.2021.04.003. [PubMed: 33932339]

3. Damkier HH, Brown PD, and Praetorius J (2013). Cerebrospinal fluid secretion by the choroid plexus. Physiol Rev 93, 1847–1892. 10.1152/physrev.00004.2013. [PubMed: 24137023]

4. Cui J, Shipley FB, Shannon ML, Alturkistani O, Dani N, Webb MD, Sugden AU, Andermann ML, and Lehtinen MK (2020). Inflammation of the Embryonic Choroid Plexus Barrier following Maternal Immune Activation. Dev Cell 55, 617–628 e616. 10.1016/j.devcel.2020.09.020. [PubMed: 33038331]

5. Engelhardt B, Vajkoczy P, and Weller RO (2017). The movers and shapers in immune privilege of the CNS. Nat Immunol 18, 123–131. 10.1038/ni.3666. [PubMed: 28092374]

6. Reboldi A, Coisne C, Baumjohann D, Benvenuto F, Bottinelli D, Lira S, Uccelli A, Lanzavecchia A, Engelhardt B, and Sallusto F (2009). C-C chemokine receptor 6-regulated entry of TH-17 cells into the CNS through the choroid plexus is required for the initiation of EAE. Nat Immunol 10, 514–523. 10.1038/ni.1716. [PubMed: 19305396]

7. Schwartz M, and Baruch K (2014). The resolution of neuroinflammation in neurodegeneration: leukocyte recruitment via the choroid plexus. EMBO J 33, 7–22. 10.1002/embj.201386609. [PubMed: 24357543]

8. Rodriguez-Lorenzo S, Konings J, van der Pol S, Kamermans A, Amor S, van Horssen J, Witte ME, Kooij G, and de Vries HE (2020). Inflammation of the choroid plexus in progressive multiple sclerosis: accumulation of granulocytes and T cells. Acta Neuropathol Commun 8, 9. 10.1186/s40478-020-0885-1. [PubMed: 32014066]

9. Coulter IC, Dewan MC, Tailor J, Ibrahim GM, and Kulkarni AV (2021). Endoscopic third ventriculostomy and choroid plexus cauterization (ETV/CPC) for hydrocephalus of infancy: a technical review. Childs Nerv Syst 37, 3509–3519. 10.1007/s00381-021-05209-5. [PubMed: 33991213]

10. Kahle KT, Kulkarni AV, Limbrick DD Jr., and Warf BC (2016). Hydrocephalus in children. Lancet 387, 788–799. 10.1016/S0140-6736(15)60694-8. [PubMed: 26256071]

11. Warf BC (2005). Comparison of endoscopic third ventriculostomy alone and combined with choroid plexus cauterization in infants younger than 1 year of age: a prospective study in 550 African children. J Neurosurg 103, 475–481. 10.3171/ped.2005.103.6.0475. [PubMed: 16383244]

12. Anderson IA, Saukila LF, Robins JMW, Akhunbay-Fudge CY, Goodden JR, Tyagi AK, Phillips N, and Chumas PD (2018). Factors associated with 30-day ventriculoperitoneal shunt failure in pediatric and adult patients. J Neurosurg 130, 145–153. 10.3171/2017.8.JNS17399. [PubMed: 29521592]

13. Kulkarni AV, Riva-Cambrin J, Butler J, Browd SR, Drake JM, Holubkov R, Kestle JR, Limbrick DD, Simon TD, Tamber MS, et al. (2013). Outcomes of CSF shunting in children: comparison of Hydrocephalus Clinical Research Network cohort with historical controls: clinical article. J Neurosurg Pediatr 12, 334–338. 10.3171/2013.7.PEDS12637. [PubMed: 23909616]

14. Karimy JK, Reeves BC, Damisah E, Duy PQ, Antwi P, David W, Wang K, Schiff SJ, Limbrick DD Jr., Alper SL, et al. (2020). Inflammation in acquired hydrocephalus: pathogenic mechanisms and therapeutic targets. Nat Rev Neurol 16, 285–296. 10.1038/s41582-020-0321-y. [PubMed: 32152460]

15. Fleischer V, Gonzalez-Escamilla G, Ciolac D, Albrecht P, Kury P, Gruchot J, Dietrich M, Hecker C, Muntefering T, Bock S, et al. (2021). Translational value of choroid plexus imaging for tracking neuroinflammation in mice and humans. Proc Natl Acad Sci U S A 118. 10.1073/pnas.2025000118.

16. Shipley FB, Dani N, Xu H, Deister C, Cui J, Head JP, Sadegh C, Fame RM, Shannon ML, Flores VI, et al. (2020). Tracking Calcium Dynamics and Immune Surveillance at the Choroid Plexus Blood-Cerebrospinal Fluid Interface. Neuron 108, 623–639 e610. 10.1016/j.neuron.2020.08.024. [PubMed: 32961128]

17. Muller J, Sinnecker T, Wendebourg MJ, Schlager R, Kuhle J, Schadelin S, Benkert P, Derfuss T, Cattin P, Jud C, et al. (2022). Neurol Neuroimmunol Neuroinflamm 9. 10.1212/NXI.0000000000001147.

18. Symss NP, and Oi S (2013). J Neurosurg Pediatr 11, 170–177. 10.3171/2012.3.PEDS0934. [PubMed: 23215851]

19. Habiyaremye G, Morales DM, Morgan CD, McAllister JP, CreveCoeur TS, Han RH, Gabir M, Baksh B, Mercer D, and Limbrick DD Jr. (2017). Fluids Barriers CNS 14, 35. 10.1186/s12987-017-0083-0. [PubMed: 29228970]

20. Lepennetier G, Hracsko Z, Unger M, Van Griensven M, Grummel V, Krumbholz M, Berthele A, Hemmer B, and Kowarik MC (2019). J Neuroinflammation 16, 219. 10.1186/s12974-019-1601-6. [PubMed: 31727097]

21. Cuoco JA, Guilliams EL, Klein BJ, Benko MJ, Darden JA, Olasunkanmi AL, Witcher MR, Rogers CM, Marvin EA, Patel BM, and Entwistle JJ (2021). World Neurosurg 156, e338–e344. 10.1016/j.wneu.2021.09.059. [PubMed: 34555578]

22. Berkes J, Viswanathan VK, Savkovic SD, and Hecht G (2003). Gut 52, 439–451. 10.1136/gut.52.3.439. [PubMed: 12584232]

23. Doyle WJ, Skoner DP, Hayden F, Buchman CA, Seroky JT, and Fireman P (1994). Ann Otol Rhinol Laryngol 103, 59–69. 10.1177/000348949410300111. [PubMed: 8291861]

24. Wilson R, Alton E, Rutman A, Higgins P, Al Nakib W, Geddes DM, Tyrrell DA, and Cole PJ (1987). Eur J Respir Dis 70, 272–279. [PubMed: 3609187]

25. Yan Y, Dalmasso G, Nguyen HT, Obertone TS, Charrier-Hisamuddin L, Sitaraman SV, and Merlin D (2008). Am J Pathol 173, 1013–1028. 10.2353/ajpath.2008.080339. [PubMed: 18787102]

26. Shekarabi M, Zhang J, Khanna AR, Ellison DH, Delpire E, and Kahle KT (2017). Cell Metab 25, 285–299. 10.1016/j.cmet.2017.01.007. [PubMed: 28178566]

27. Yan Y, Nguyen H, Dalmasso G, Sitaraman SV, and Merlin D (2007). Biochim Biophys Acta 1769, 106–116. 10.1016/j.bbaexp.2007.01.003. [PubMed: 17321610]

28. Weidenfeld S, and Kuebler WM (2017). Front Immunol 8, 393. 10.3389/fimmu.2017.00393. [PubMed: 28439270]

29. Gram M, Sveinsdottir S, Cinthio M, Sveinsdottir K, Hansson SR, Morgelin M, Akerstrom B, and Ley D (2014). J Neuroinflammation 11, 200. 10.1186/s12974-014-0200-9. [PubMed: 25441622]

30. Karimy JK, Zhang J, Kurland DB, Theriault BC, Duran D, Stokum JA, Furey CG, Zhou X, Mansuri MS, Montejo J, et al. (2017). Nat Med 23, 997–1003. 10.1038/nm.4361. [PubMed: 28692063]

31. Purohit D, Finkel DA, Malfa A, Liao Y, Ivanova L, Kleinman GM, Hu F, Shah S, Thompson C, Joseph E, et al. (2021). Front Cell Neurosci 15, 633185. 10.3389/fncel.2021.633185. [PubMed: 33897371]

32. Simard PF, Tosun C, Melnichenko L, Ivanova S, Gerzanich V, and Simard JM (2011). Transl Stroke Res 2, 227–231. 10.1007/s12975-011-0070-8. [PubMed: 21731590]

33. Tan X, Chen J, Keep RF, Xi G, and Hua Y (2020). Stroke 51, 1578–1586. 10.1161/STROKEAHA.119.028672. [PubMed: 32279622]

34. Guillen-Pinto D, Malaga-Espinoza B, Ye-Tay J, Rospigliosi-Lopez ML, Montenegro-Rivera A, Rivas M, Stiglich ML, Villasante-Valera S, Lizama-Olaya O, Tori A, et al. (2020). Rev Peru Med Exp Salud Publica 37, 210–219. 10.17843/rpmesp.2020.372.4772. [PubMed: 32876208]

35. Huo L, Fan Y, Jiang C, Gao J, Yin M, Wang H, Yang F, and Cao Q (2019). J Child Neurol 34, 11–16. 10.1177/0883073818799155. [PubMed: 30373442]

36. Li L, Padhi A, Ranjeva SL, Donaldson SC, Warf BC, Mugamba J, Johnson D, Opio Z, Jayarao B, Kapur V, et al. (2011). J Neurosurg Pediatr 7, 73–87. 10.3171/2010.9.PEDS10162. [PubMed: 21194290]

37. Hoshino K, Takeuchi O, Kawai T, Sanjo H, Ogawa T, Takeda Y, Takeda K, and Akira S (1999). J Immunol 162, 3749–3752. [PubMed: 10201887]

38. Park BS, and Lee JO (2013). Exp Mol Med 45, e66. 10.1038/emm.2013.97. [PubMed: 24310172]

39. Janciauskiene S, Vijayan V, and Immenschuh S (2020). Front Immunol 11, 1964. 10.3389/fimmu.2020.01964. [PubMed: 32983129]

40. Kwon MS, Woo SK, Kurland DB, Yoon SH, Palmer AF, Banerjee U, Iqbal S, Ivanova S, Gerzanich V, and Simard JM (2015). Int J Mol Sci 16, 5028–5046. 10.3390/ijms16035028. [PubMed: 25751721]

41. Shemie S, Jay V, Rutka J, and Armstrong D (1997). Ann Emerg Med 29, 524–528. 10.1016/s0196-0644(97)70227-0. [PubMed: 9095015]

42. Zhang J, Bhuiyan MIH, Zhang T, Karimy JK, Wu Z, Fiesler VM, Zhang J, Huang H, Hasan MN, Skrzypiec AE, et al. (2020). Nat Commun 11, 78. 10.1038/s41467-019-13851-6. [PubMed: 31911626]

43. Sarica C, Tanrikulu B, Sahin Y, Dagcinar A, Baltacioglu F, and Bayri Y (2018). Pediatr Neurosurg 53, 247–253. 10.1159/000488458. [PubMed: 29719303]

44. Xue Y, Liu X, Koundal S, Constantinou S, Dai F, Santambrogio L, Lee H, and Benveniste H (2020). Sci Rep 10, 14592. 10.1038/s41598-020-71582-x. [PubMed: 32884041]

45. Xue Y, Gursky Z, Monte B, Koundal S, Liu X, Lee H, Michurina TV, Mellanson KA, Zhao L, Nemajerova A, et al. (2022). Fluids Barriers CNS 19, 20. 10.1186/s12987-022-00319-x. [PubMed: 35248089]

46. Thalen S, Maanja M, Sigfridsson A, Maret E, Sorensson P, and Ugander M (2019). J Cardiovasc Magn Reson 21, 71. 10.1186/s12968-019-0580-1. [PubMed: 31730498]

47. Chen X, Liu X, Koundal S, Elkin R, Zhu X, Monte B, Xu F, Dai F, Pedram M, Lee H, et al. (2022). Nat Aging 2, 214–223. 10.1038/s43587-022-00181-4. [PubMed: 36199752]

48. Zhao L, Tannenbaum A, Bakker E, and Benveniste H (2022). Physiology (Bethesda) 37, 0. 10.1152/physiol.00015.2022.

49. Proulx ST (2021). Cell Mol Life Sci 78, 2429–2457. 10.1007/s00018-020-03706-5. [PubMed: 33427948]

50. Hladky SB, and Barrand MA (2022). Fluids Barriers CNS 19, 9. 10.1186/s12987-021-00282-z. [PubMed: 35115036]

51. Doctor BA, Newman N, Minich NM, Taylor HG, Fanaroff AA, and Hack M (2001). Clin Pediatr (Phila) 40, 473–480. 10.1177/000992280104000901. [PubMed: 11583045]

52. Deopujari CE, Padayachy L, Azmi A, Figaji A, and Samantray SK (2018). Childs Nerv Syst 34, 1905–1914. 10.1007/s00381-018-3901-z. [PubMed: 30099619]

53. Karimy JK, Kahle KT, Kurland DB, Yu E, Gerzanich V, and Simard JM (2015). J Neurosci Methods 241, 78–84. 10.1016/j.jneumeth.2014.12.015. [PubMed: 25554415]

54. Liu G, Mestre H, Sweeney AM, Sun Q, Weikop P, Du T, and Nedergaard M (2020). Cell Rep 33, 108524. 10.1016/j.celrep.2020.108524. [PubMed: 33357428]

55. Javaheri S, and Wagner KR (1993). In vivo evidence for NaCl cotransport in the central nervous system. J Clin Invest 92, 2257–2261. 10.1172/JCI116829. [PubMed: 8227341]

56. Karimy JK, Duran D, Hu JK, Gavankar C, Gaillard JR, Bayri Y, Rice H, DiLuna ML, Gerzanich V, Marc Simard J, and Kahle KT (2016). Neurosurg Focus 41, E10. 10.3171/2016.8.FOCUS16278.

57. Ferguson C, McKay M, Harris RA, and Homanics GE (2013). Alcohol 47, 595–599. 10.1016/j.alcohol.2013.09.043. [PubMed: 24199847]

58. Van Hove H, Martens L, Scheyltjens I, De Vlaminck K, Pombo Antunes AR, De Prijck S, Vandamme N, De Schepper S, Van Isterdael G, Scott CL, et al. (2019). Nat Neurosci 22, 1021–1035. 10.1038/s41593-019-0393-4. [PubMed: 31061494]

59. Karman J, Chu HH, Co DO, Seroogy CM, Sandor M, and Fabry Z (2006). J Immunol 177, 7750–7760. 10.4049/jimmunol.177.11.7750. [PubMed: 17114446]

60. McWhorter FY, Wang T, Nguyen P, Chung T, and Liu WF (2013). Proc Natl Acad Sci U S A 110, 17253–17258. 10.1073/pnas.1308887110. [PubMed: 24101477]

61. Chistiakov DA, Killingsworth MC, Myasoedova VA, Orekhov AN, and Bobryshev YV (2017). Lab Invest 97, 4–13. 10.1038/labinvest.2016.116.

62. Dodge PR, and Swartz MN (1965). Ii. Special Neurologic Problems, Postmeningitic Complications and Clinicopathological Correlations. N Engl J Med 272, 1003–1010 CONCL. 10.1056/NEJM196505132721906. [PubMed: 14279246]

63. Vergouwen MD, Schut ES, Troost D, and van de Beek D (2010). Neurocrit Care 13, 217–227. 10.1007/s12028-010-9387-5. [PubMed: 20526697]

64. Dickson LG, and Yassin MW (1969). J Egypt Public Health Assoc 44, 349–355. [PubMed: 5377725]

65. Engelen-Lee JY, Brouwer MC, Aronica E, and van de Beek D (2016). Acta Neuropathol Commun 4, 26. 10.1186/s40478-016-0297-4. [PubMed: 27001057]

66. Nakano A, Harada T, Morikawa S, and Kato Y (1990). Acta Pathol Jpn 40, 107–115. 10.1111/j.1440-1827.1990.tb01549.x. [PubMed: 2140233]

67. Rangaraju S, Raza SA, Li NX, Betarbet R, Dammer EB, Duong D, Lah JJ, Seyfried NT, and Levey AI (2018). Front Immunol 9, 405. 10.3389/fimmu.2018.00405. [PubMed: 29552013]

68. Sharma S, Goyal MK, Sharma K, Modi M, Sharma M, Khandelwal N, Prabhakar S, Sharma N, R S, Gairolla J, et al. (2017). J Neurol Sci 379, 131–136. 10.1016/j.jns.2017.06.001. [PubMed: 28716226]

69. Thwaites GE, Macmullen-Price J, Tran TH, Pham PM, Nguyen TD, Simmons CP, White NJ, Tran TH, Summers D, and Farrar JJ (2007). Lancet Neurol 6, 230–236. 10.1016/S1474-4422(07)70034-0. [PubMed: 17303529]

70. Lolansen SD, Rostgaard N, Oernbo EK, Juhler M, Simonsen AH, and MacAulay N (2021). Dis Markers 2021, 8834822. 10.1155/2021/8834822. [PubMed: 33613789]

71. Vitari AC, Thastrup J, Rafiqi FH, Deak M, Morrice NA, Karlsson HK, and Alessi DR (2006). Biochem J 397, 223–231. 10.1042/BJ20060220. [PubMed: 16669787]

72. Vitari AC, Deak M, Morrice NA, and Alessi DR (2005). Biochem J 391, 17–24. 10.1042/BJ20051180. [PubMed: 16083423]

73. Yan Y, and Merlin D (2008). World J Gastroenterol 14, 6115–6121. 10.3748/wjg.14.6115. [PubMed: 18985800]

74. Polek TC, Talpaz M, and Spivak-Kroizman T (2006). Biochem Biophys Res Commun 343, 125–134. 10.1016/j.bbrc.2006.02.125. [PubMed: 16530727]

75. Delpire E, and Gagnon KB (2008). Biochem J 409, 321–331. 10.1042/BJ20071324. [PubMed: 18092945]

76. Richardson C, and Alessi DR (2008). J Cell Sci 121, 3293–3304. 10.1242/jcs.029223. [PubMed: 18843116]

77. Dwinell MR, Lazar J, and Geurts AM (2011). Mamm Genome 22, 466–475. 10.1007/s00335-011-9346-2. [PubMed: 21732192]

78. Savman K, Blennow M, Hagberg H, Tarkowski E, Thoresen M, and Whitelaw A (2002). Acta Paediatr 91, 1357–1363. 10.1111/j.1651-2227.2002.tb02834.x. [PubMed: 12578295]

79. Schmitz T, Heep A, Groenendaal F, Huseman D, Kie S, Bartmann P, Obladen M, and Felderhoff-Muser U (2007). 10.1203/pdr.0b013e31805341f1.

80. Figueiredo RT, Fernandez PL, Mourao-Sa DS, Porto BN, Dutra FF, Alves LS, Oliveira MF, Oliveira PL, Graca-Souza AV, and Bozza MT (2007). J Biol Chem 282, 20221–20229. 10.1074/jbc.M610737200. [PubMed: 17502383]

81. Molteni M, Gemma S, and Rossetti C (2016). Mediators Inflamm 2016, 6978936. 10.1155/2016/6978936. [PubMed: 27293318]

82. Jin S, Guerrero-Juarez CF, Zhang L, Chang I, Ramos R, Kuan CH, Myung P, Plikus MV, and Nie Q (2021). Nat Commun 12, 1088. 10.1038/s41467-021-21246-9. [PubMed: 33597522]

83. Kim J, Erikson DW, Burghardt RC, Spencer TE, Wu G, Bayless KJ, Johnson GA, and Bazer FW (2010). Matrix Biol 29, 369–382. 10.1016/j.matbio.2010.04.001. [PubMed: 20385232]

84. Bazer FW, Song G, Kim J, Erikson DW, Johnson GA, Burghardt RC, Gao H, Carey Satterfield M, Spencer TE, and Wu G (2012). Mol Cell Endocrinol 354, 22–33. 10.1016/j.mce.2011.08.026. [PubMed: 21907263]

85. Anwar MA, Shah M, Kim J, and Choi S (2019). Med Res Rev 39, 1053–1090. 10.1002/med.21553. [PubMed: 30450666]

86. Josiah SS, Meor Azlan NF, and Zhang J (2021). Int J Mol Sci 22. 10.3390/ijms22031232.

87. Nishida H, Sohara E, Nomura N, Chiga M, Alessi DR, Rai T, Sasaki S, and Uchida S (2012). Hypertension 60, 981–990. 10.1161/HYPERTENSIONAHA.112.201509. [PubMed: 22949526]

88. Sorensen MV, Saha B, Jensen IS, Wu P, Ayasse N, Gleason CE, Svendsen SL, Wang WH, and Pearce D (2019). JCI Insight 5. 10.1172/jci.insight.126910.

89. Weichhart T, Hengstschlager M, and Linke M (2015). Nat Rev Immunol 15, 599–614. 10.1038/nri3901. [PubMed: 26403194]

90. Xu F, Na L, Li Y, and Chen L (2020). Cell Biosci 10, 54. 10.1186/s13578-020-00416-0. [PubMed: 32266056]

91. Robert SM, Reeves BC, Marlier A, Duy PQ, DeSpenza T, Kundishora A, Kiziltug E, Singh A, Allington G, Alper SL, and Kahle KT (2021). Childs Nerv Syst 37, 3341–3353. 10.1007/s00381-021-05255-z. [PubMed: 34164718]

92. Garoon RB, Foroozan R, and Vaphiades MS (2017). Surv Ophthalmol 62, 383–386. 10.1016/j.survophthal.2016.04.002. [PubMed: 27102841]

93. Stone SS, and Warf BC (2014). J Neurosurg Pediatr 14, 439–446. 10.3171/2014.7.PEDS14152. [PubMed: 25171723]

94. Buxton N, and Punt J (1997). Pediatr Neurosurg 27, 108–111. 10.1159/000121236. [PubMed: 9520084]

95. Eisenberg HM, McComb JG, and Lorenzo AV (1974). J Neurosurg 40, 381–385. 10.3171/ jns.1974.40.3.0381. [PubMed: 4544345]

96. Milhorat TH, Hammock MK, Davis DA, and Fenstermacher JD (1976). I. Proof of cerebrospinal fluid overproduction. Childs Brain 2, 273–289. [PubMed: 1022421]

97. Anei R, Hayashi Y, Hiroshima S, Mitsui N, Orimoto R, Uemori G, Saito M, Sato M, Wada H, Hododuka A, and Kamada K (2011). Neurol Med Chir (Tokyo) 51, 437–441. 10.2176/nmc.51.437. [PubMed: 21701109]

98. Cataltepe O, Liptzin D, Jolley L, and Smith TW (2010). J Neurosurg Pediatr 5, 518–522. 10.3171/2009.12.PEDS0960. [PubMed: 20433267]

99. Furey C, Antwi P, Duran D, Timberlake AT, Nelson-Williams C, Matouk CC, DiLuna ML, Gunel M, and Kahle KT (2018). Cold Spring Harb Mol Case Stud 4. 10.1101/mcs.a003145.

100. Jin SC, Dong W, Kundishora AJ, Panchagnula S, Moreno-De-Luca A, Furey CG, Allocco AA, Walker RL, Nelson-Williams C, Smith H, et al. (2020). Nat Med 26, 1754–1765. 10.1038/ s41591-020-1090-2. [PubMed: 33077954]

101. Erickson MA, Hartvigson PE, Morofuji Y, Owen JB, Butterfield DA, and Banks WA (2012). J Neuroinflammation 9, 150. 10.1186/1742-2094-9-150. [PubMed: 22747709]

102. Manouchehrian O, Ramos M, Bachiller S, Lundgaard I, and Deierborg T (2021). J Neuroinflammation 18, 34. 10.1186/s12974-021-02082-6. [PubMed: 33514389]

103. Fratamico PM, DebRoy C, Liu Y, Needleman DS, Baranzoni GM, and Feng P (2016). Front Microbiol 7, 644. 10.3389/fmicb.2016.00644. [PubMed: 27199968]

104. Kaczmarek A, Budzynska A, and Gospodarek E (2014). Folia Microbiol (Praha) 59, 419–422. 10.1007/s12223-014-0315-5. [PubMed: 24737297]

105. Hu X, Deng Q, Ma L, Li Q, Chen Y, Liao Y, Zhou F, Zhang C, Shao L, Feng J, et al. (2020). Cell Res 30, 229–243. 10.1038/s41422-020-0287-8. [PubMed: 32094452]

106. Papadopoulos Z, Herz J, and Kipnis J (2020). J Immunol 204, 286–293. 10.4049/ jimmunol.1900838. [PubMed: 31907271]

107. Hajam IA, Dar PA, Shahnawaz I, Jaume JC, and Lee JH (2017). Exp Mol Med 49, e373. 10.1038/ emm.2017.172. [PubMed: 28860663]

108. Engelhardt B, Wolburg-Buchholz K, and Wolburg H (2001). Microsc Res Tech 52, 112–129. 10.1002/1097-0029(20010101)52:1<112::AID-JEMT13>3.0.CO;2-5. [PubMed: 11135454]

109. Ghersi-Egea JF, Strazielle N, Catala M, Silva-Vargas V, Doetsch F, and Engelhardt B (2018). Acta Neuropathol 135, 337–361. 10.1007/s00401-018-1807-1. [PubMed: 29368213]

110. Gu C, Hao X, Li J, Hua Y, Keep RF, and Xi G (2019). J Cereb Blood Flow Metab 39, 1936–1948. 10.1177/0271678X19836117. [PubMed: 30862302]

111. Stridh L, Ek CJ, Wang X, Nilsson H, and Mallard C (2013). Transl Stroke Res 4, 220–227. 10.1007/s12975-012-0248-8. [PubMed: 23741282]

112. Shimada A, and Hasegawa-Ishii S (2021). Toxicol Rep 8, 520–528. 10.1016/j.toxrep.2021.03.002. [PubMed: 33747797]

113. Akira S, and Takeda K (2004). Nat Rev Immunol 4, 499–511. 10.1038/nri1391. [PubMed: 15229469]

114. Laird MD, Shields JS, Sukumari-Ramesh S, Kimbler DE, Fessler RD, Shakir B, Youssef P, Yanasak N, Vender JR, and Dhandapani KM (2014). Glia 62, 26–38. 10.1002/glia.22581. [PubMed: 24166800]

115. Chen T, Tan X, Xia F, Hua Y, Keep RF, and Xi G (2021). Biomolecules 11. 10.3390/ biom11050654.

116. Merle NS, Paule R, Leon J, Daugan M, Robe-Rybkine T, Poillerat V, Torset C, Fremeaux-Bacchi V, Dimitrov JD, and Roumenina LT (2019). Proc Natl Acad Sci U S A 116, 6280–6285. 10.1073/ pnas.1814797116. [PubMed: 30850533]

117. Nader E, Romana M, and Connes P (2020). Front Immunol 11, 454. 10.3389/fimmu.2020.00454. [PubMed: 32231672]

118. Haas J, Rudolph H, Costa L, Faller S, Libicher S, Wurthwein C, Jarius S, Ishikawa H, Stump-Guthier C, Tenenbaum T, et al. (2020). Front Immunol 11, 618544. 10.3389/fimmu.2020.618544. [PubMed: 33574821]

119. Kim H, Lim YM, Kim G, Lee EJ, Lee JH, Kim HW, and Kim KK (2020). J Neurol Sci 415, 116904. 10.1016/j.jns.2020.116904. [PubMed: 32446012]

120. Yan Y, Dalmasso G, Nguyen HT, Obertone TS, Sitaraman SV, and Merlin D (2009). PLoS One 4, e5049. 10.1371/journal.pone.0005049. [PubMed: 19343169]

121. Yan Y, Laroui H, Ingersoll SA, Ayyadurai S, Charania M, Yang S, Dalmasso G, Obertone TS, Nguyen H, Sitaraman SV, and Merlin D (2011). J Immunol 187, 1496–1505. 10.4049/jimmunol.1002910. [PubMed: 21705622]

122. Alessi DR, Zhang J, Khanna A, Hochdorfer T, Shang Y, and Kahle KT (2014). Sci Signal 7, re3. 10.1126/scisignal.2005365. [PubMed: 25028718]

123. Chaplin ER, Goldstein GW, Myerberg DZ, Hunt JV, and Tooley WH (1980). Pediatrics 65, 901–909. [PubMed: 7367137]

124. Steffensen AB, Oernbo EK, Stoica A, Gerkau NJ, Barbuskaite D, Tritsaris K, Rose CR, and MacAulay N (2018). Nat Commun 9, 2167. 10.1038/s41467-018-04677-9. [PubMed: 29867199]

125. Stodberg T, Magnusson M, Lesko N, Wredenberg A, Martin Munoz D, Stranneheim H, and Wedell A (2020). Neurol Genet 6, e478. 10.1212/NXG.0000000000000478. [PubMed: 32754646]

126. Xu H, Fame RM, Sadegh C, Sutin J, Naranjo C, Della S, Cui J, Shipley FB, Vernon A, Gao F, et al. (2021). Nat Commun 12, 447. 10.1038/s41467-020-20666-3. [PubMed: 33469018]

127. Thastrup JO, Rafiqi FH, Vitari AC, Pozo-Guisado E, Deak M, Mehellou Y, and Alessi DR (2012). Biochem J 441, 325–337. 10.1042/BJ20111879. [PubMed: 22032326]

128. Karimy JK, Reeves BC, and Kahle KT (2020). Expert Opin Ther Targets 24, 525–533. 10.1080/14728222.2020.1752182. [PubMed: 32249624]

129. Matsunaga N, Tsuchimori N, Matsumoto T, and Ii M (2011). Mol Pharmacol 79, 34–41. 10.1124/mol.110.068064. [PubMed: 20881006]

130. Kotani T, Setiawan J, Konno T, Ihara N, Okamoto S, Saito Y, Murata Y, Noda T, and Matozaki T (2020). Sci Rep 10, 13810. 10.1038/s41598-020-70655-1. [PubMed: 32796887]

131. Zhou M, Xu W, Wang J, Yan J, Shi Y, Zhang C, Ge W, Wu J, Du P, and Chen Y (2018). EBioMedicine 35, 345–360. 10.1016/j.ebiom.2018.08.035. [PubMed: 30170968]

132. Yu M, Kang X, Xue H, and Yin H (2011). Acta Biochim Biophys Sin (Shanghai) 43, 940–947. 10.1093/abbs/gmr093. [PubMed: 22015781]

133. Sengupta S, Lorente-Rodriguez A, Earnest S, Stippec S, Guo X, Trudgian DC, Mirzaei H, and Cobb MH (2013). Proc Natl Acad Sci U S A 110, 18826–18831. 10.1073/pnas.1318676110. [PubMed: 24191005]

134. Krueger DA, Care MM, Holland K, Agricola K, Tudor C, Mangeshkar P, Wilson KA, Byars A, Sahmoud T, and Franz DN (2010). N Engl J Med 363, 1801–1811. 10.1056/NEJMoa1001671. [PubMed: 21047224]

135. Li J, Kim SG, and Blenis J (2014). Cell Metab 19, 373–379. 10.1016/j.cmet.2014.01.001. [PubMed: 24508508]

136. Ye X, Zhu M, Che X, Wang H, Liang XJ, Wu C, Xue X, and Yang J (2020). J Neuroinflammation 17, 18. 10.1186/s12974-019-1644-8. [PubMed: 31926553]

137. Mengke NS, Hu B, Han QP, Deng YY, Fang M, Xie D, Li A, and Zeng HK (2016). Mol Med Rep 14, 4957–4966. 10.3892/mmr.2016.5883. [PubMed: 27779711]

138. Lodhia KR, Shakui P, and Keep RF (2006). Acta Neurochir Suppl 96, 207–211. 10.1007/3-211-30714-1_45. [PubMed: 16671456]

139. Perez-Riverol Y, Csordas A, Bai J, Bernal-Llinares M, Hewapathirana S, Kundu DJ, Inuganti A, Griss J, Mayer G, Eisenacher M, et al. (2019). Nucleic Acids Res 47, D442–D450. 10.1093/nar/gky1106. [PubMed: 30395289]

140. Garate I, Garcia-Bueno B, Madrigal JL, Caso JR, Alou L, Gomez-Lus ML, and Leza JC (2014). J Neuroinflammation 11, 8. 10.1186/1742-2094-11-8. [PubMed: 24410883]

141. Schindelin J, Arganda-Carreras I, Frise E, Kaynig V, Longair M, Pietzsch T, Preibisch S, Rueden C, Saalfeld S, Schmid B, et al. (2012). Nat Methods 9, 676–682. 10.1038/nmeth.2019. [PubMed: 22743772]

142. Zhang J, Gao G, Begum G, Wang J, Khanna AR, Shmukler BE, Daubner GM, de Los Heros P, Davies P, Varghese J, et al. (2016). Sci Rep 6, 35986. 10.1038/srep35986. [PubMed: 27782176]

143. Anders S, Pyl PT, and Huber W (2015). Bioinformatics 31, 166–169. 10.1093/bioinformatics/btu638. [PubMed: 25260700]

144. Love MI, Huber W, and Anders S (2014). Genome Biol 15, 550. 10.1186/s13059-014-0550-8. [PubMed: 25516281]

145. Gu Z, Eils R, and Schlesner M (2016). Bioinformatics 32, 2847–2849. 10.1093/bioinformatics/btw313. [PubMed: 27207943]

146. Lee AM, Mansuri MS, Wilson RS, Lam TT, Nairn AC, and Picciotto MR (2021). Front Mol Neurosci 14, 657064. 10.3389/fnmol.2021.657064. [PubMed: 34335180]

147. McAlister GC, Nusinow DP, Jedrychowski MP, Wuhr M, Huttlin EL, Erickson BK, Rad R, Haas W, and Gygi SP (2014). Anal Chem 86, 7150–7158. 10.1021/ac502040v. [PubMed: 24927332]

148. Miller MB, Wilson RS, Lam TT, Nairn AC, and Picciotto MR (2018). Proteomes 6. 10.3390/proteomes6040042.

149. Janostiak R, Rauniyar N, Lam TT, Ou J, Zhu LJ, Green MR, and Wajapeyee N (2017). Cell Rep 21, 2829–2841. 10.1016/j.celrep.2017.11.033. [PubMed: 29212029]

150. Hao Y, Hao S, Andersen-Nissen E, Mauck WM 3rd, Zheng S, Butler A, Lee MJ, Wilk AJ, Darby C, Zager M, et al. (2021). Cell 184, 3573–3587 e3529. 10.1016/j.cell.2021.04.048. [PubMed: 34062119]

151. Montoro DT, Haber AL, Biton M, Vinarsky V, Lin B, Birket SE, Yuan F, Chen S, Leung HM, Villoria J, et al. (2018). Nature 560, 319–324. 10.1038/s41586-018-0393-7. [PubMed: 30069044]

152. Becht E, McInnes L, Healy J, Dutertre CA, Kwok IWH, Ng LG, Ginhoux F, and Newell EW (2018). Nat Biotechnol. 10.1038/nbt.4314.

153. McGinnis CS, Murrow LM, and Gartner ZJ (2019). Cell Syst 8, 329–337 e324. 10.1016/j.cels.2019.03.003. [PubMed: 30954475]

154. Cao J, Spielmann M, Qiu X, Huang X, Ibrahim DM, Hill AJ, Zhang F, Mundlos S, Christiansen L, Steemers FJ, et al. (2019). Nature 566, 496–502. 10.1038/s41586-019-0969-x. [PubMed: 30787437]

155. Federico A, and Monti S (2020). Bioinformatics 36, 1307–1308. 10.1093/bioinformatics/btz700. [PubMed: 31498385]

156. Kuleshov MV, Jones MR, Rouillard AD, Fernandez NF, Duan Q, Wang Z, Koplev S, Jenkins SL, Jagodnik KM, Lachmann A, et al. (2016). Nucleic Acids Res 44, W90–97. 10.1093/nar/gkw377. [PubMed: 27141961]

157. Tustison NJ, Avants BB, Cook PA, Zheng Y, Egan A, Yushkevich PA, and Gee JC (2010). IEEE Trans Med Imaging 29, 1310–1320. 10.1109/TMI.2010.2046908. [PubMed: 20378467]

158. Koundal S, Liu X, Sanggaard S, Mortensen K, Wardlaw J, Nedergaard M, Benveniste H, and Lee H (2019). Neuroscience 404, 14–26. 10.1016/j.neuroscience.2019.01.030. [PubMed: 30690138]

159. Smith NM, Ford JN, Haghdel A, Glodzik L, Li Y, D'Angelo D, RoyChoudhury A, Wang X, Blennow K, de Leon MJ, and Ivanidze J (2022). Front Aging Neurosci 14, 849932. 10.3389/fnagi.2022.849932. [PubMed: 35547630]

160. Chen X, Liu X, Koundal S, Elkin R, Zhu X, Monte B, Xu F, Dai F, Pedram M, Lee H, et al. (2022). Nature Aging 2, 214–223. 10.1038/s43587-022-00181-4. [PubMed: 36199752]

HIGHLIGHTS

1. Integrated multi-omics study of models of infectious and hemorrhagic hydrocephalus

2. Blood or bacteria in CSF elicit highly similar ChP immune and secretory responses

3. Crosstalk between ChP immune and epithelial cells drives pathologic CSF secretion

4. Immunomodulators treat PIH/PHH by antagonizing a SPAK-regulated ChP transportome
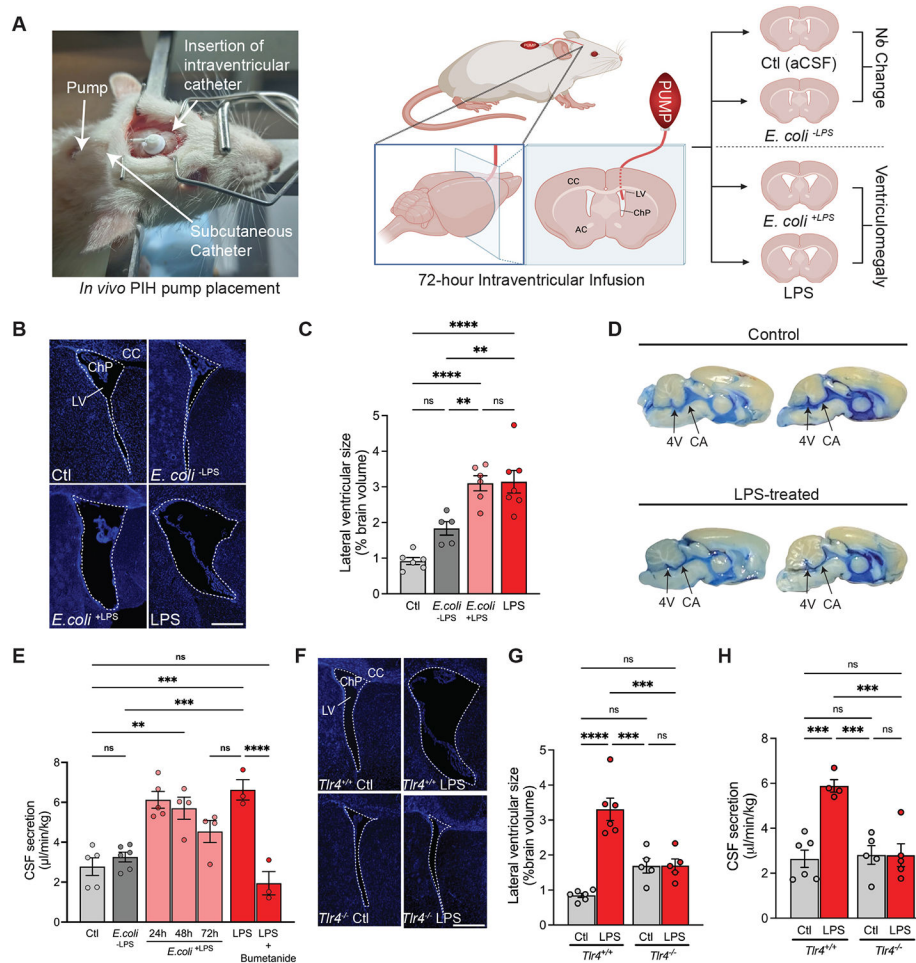
Fig. 1. Models of *E. coli* post-infectious hydrocephalus exhibit ChP-mediated CSF hypersecretion.

(A) Illustration of two models of post-infectious hydrocephalus (PIH). Insertion of an infusion pump in the lateral ventricle (LV) for *E. coli*+LPS, *E. coli*–LPS, LPS, or artificial CSF (aCSF, Ctl) administration over 72h. Left, illustration of the subcutaneous pump/ catheter and intraventricular catheter placement. Right, schematic demonstrating pump/ catheter placement and resulting ventricular changes. CC, corpus callosum, AC, anterior commissure. (B) Representative immunohistochemical images showing lateral ventricles 72h after infusion of control, *E. coli*+LPS, *E. coli*–LPS, or LPS (DAPI, blue). (C) Quantification of lateral ventricular size (% brain volume) after 72h infusion of aCSF, *E. coli*+LPS, *E. coli*–LPS, or LPS. Volume was calculated from sequential slices through the entire lateral ventricular system (n=5-7 animals per condition; see Methods). (D) Ventricular system infusion of Evans blue dye (injected into the LV of Ctl and LPS-treated animals), demonstrating flow through cerebral aqueduct (CA) and fourth ventricle (4V). (E) Body weight-normalized CSF secretion rates (μL/min/kg) in control (aCSF), *E. coli*+LPS (24h, 48h, or 72h), *E. coli*–LPS, LPS (72 h), or LPS + bumetanide (72 h)-treated animals (n=3-6 animals per condition). (F) Representative immunohistochemical images of LVs in Ctl vs LPS-treated *Tlr4*+/+ and *Tlr4*−/− rats (DAPI, blue). (G) Quantitation of LV size (% brain volume) in Ctl and LPS-treated *Tlr4*+/+ and *Tlr4*−/− rats (n=5-6 animals per condition).
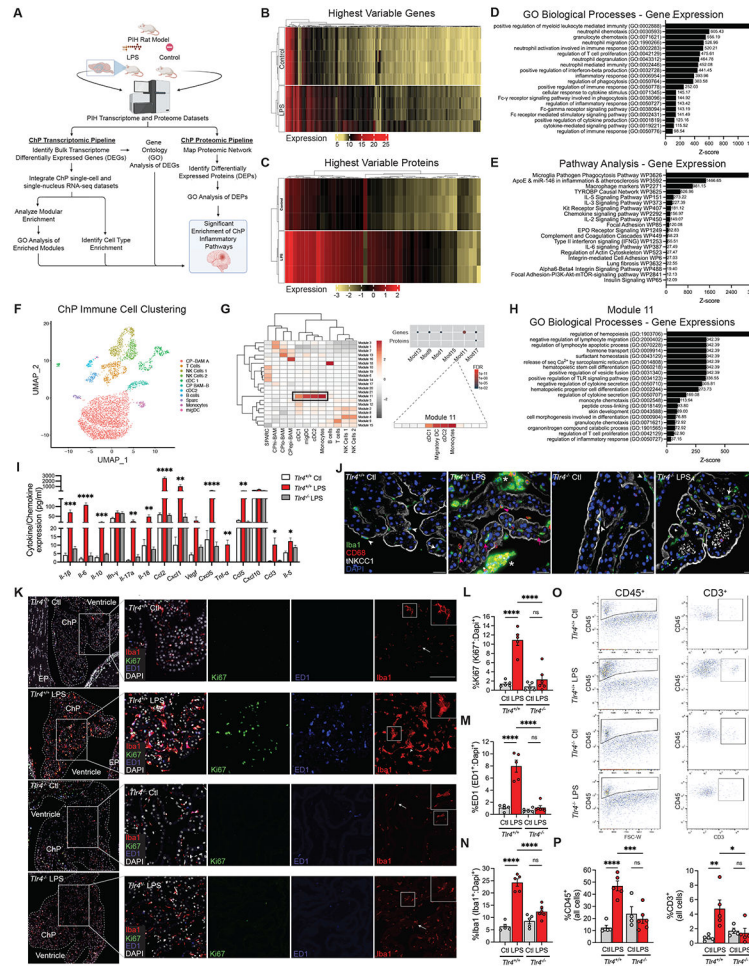
(H) Body weight-normalized CSF secretion rates (μL/min/kg) of *Tlr4*^{+/+} Ctl, *Tlr4*^{+/+} LPS-treated, *Tlr4*^{−/−} Ctl, and *Tlr4*^{−/−} LPS-treated rats (n=4-6 animals per condition). 2.5x mag, scale bars 0.25m. Error bars, mean ± sem; each symbol represents one animal. *p<0.05, **p<0.01, ***p<0.001, ****p<0.0001, ns = not significant, by one-way ANOVA.

Figure 2. Post-infectious hydrocephalus is associated with robust ChP-CSF interface inflammation.

(A) Schematic of integrated multi-omic analysis. (B-C) Heatmaps of the most highly differentially expressed ChP genes (B) and proteins (C) from LPS-treated and control rats (n=3-5 animals per condition). (D) Gene Ontology (GO) and (E) pathway analysis of differentially expressed genes (DEGs). (F) UMAP clustering of ChP immune cells and (G, left) gene expression module heatmap for individual cell types using a scRNAseq brain macrophage atlas[58]. (G, upper right) Hypergeometric enrichment analysis of LPS-induced DEGs/DEPs in gene co-expression modules (G, lower right); Module 11 gene enrichment demonstrating dendritic cell (DC) and monocyte expression. (H) Module 11 GO biological process analysis (see also Methods, Table S1*). (I) CSF cytokine/chemokine expression (pg/mL) in Ctl and LPS-treated $Tlr4^{+/+}$ and $Tlr4^{-/-}$ rats (n=3 animals per condition). (J) Representative IHC of Ctl and LPS-treated $Tlr4^{+/+}$ and $Tlr4^{-/-}$ rat ChP. Iba1^{+} (green)/CD68^{+} (red) cells located apically (epiplexus macrophages, white arrowheads) and within stroma/capillaries (white arrows); activated macrophages (pink arrowheads). Apical membrane tNkcc1 (white); nuclei (DAPI, blue); scale bars, 25μm. (K) Representative merged (left) and magnified merged and single-channel IHC (right) of Ki-67 (green), ED1 (blue), Iba1 (red), and DAPI (white) in Ctl and LPS-treated $Tlr4^{+/+}$ and $Tlr4^{-/-}$ rat ChP; senescent (arrows) and activated (arrowheads) Iba1^{+} cells. Scale bars, 50μm; insets at right, 2x enlarged. (L-N)
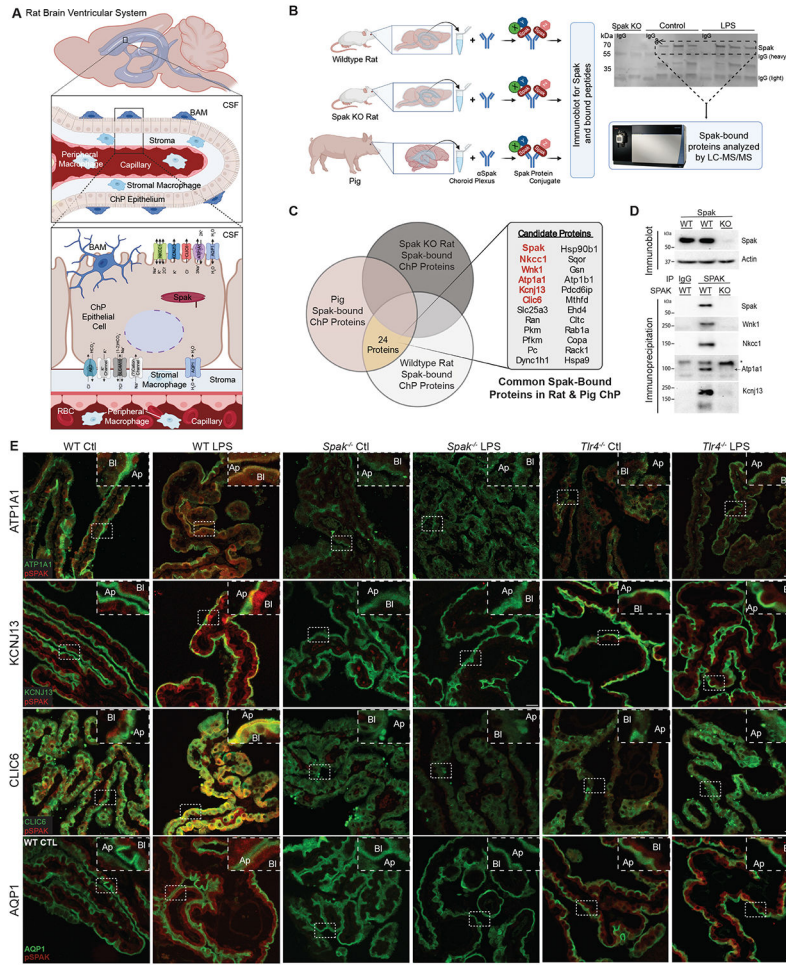
Quantitation of (K) showing DAPI-normalized % Iba1^{+} (L), ED1^{+} (M), and Ki67^{+} cells (N) (n=5-6 animals per condition). (O) Scatterplots and (P) quantitation of FACS-isolated CD45^{+} (left) and CD3^{+} ChP cells (right) (n=4-6 animals per condition). Error bars, mean ± sem; each symbol represents one animal. *p<0.05, **p<0.01, ***p<0.001, ****p<0.0001, ns = not significant, by one-way ANOVA.

Figure 3. SPAK kinase is a regulatory scaffold for an apically-localized multi-ion transporter complex in ChP epithelial cells.

(A) Schematic illustrating the rat ventricular system and ChP, highlighting important ion transporters and channels in the apical and basolateral membranes of the ChP epithelium. BAM, border-associated macrophage; CSF, cerebrospinal fluid; RBC, red blood cell. (B, left) Illustration of SPAK immunoprecipitation and LC-MS/MS analysis of SPAK-interacting proteins detected in the micro-dissected ChP of $Spak^{+/+}$ and $Spak^{-/-}$ rats, and wildtype pig (see Methods). (B, right) Western blot of SPAK, illustrating removal of gel lanes (area of the dashed box) corresponding to SPAK/SPAK-associated proteins for analysis with LC-MS/MS. (C) Identification of 24 highly SPAK-bound polypeptides, shared between $Spak^{+/+}$ rats and wild-type pig ChP, and absent from immunoprecipitates from lysates of $Spak^{-/-}$ rat ChP. (D) Immunoblot of SPAK (upper blot; beta-actin, loading control) and (lower blots) co-immunoprecipitations of SPAK with LC-MS/MS-identified SPAK-bound proteins WNK1, NKCC1, ATP1A1 (*non-specific band), and KCNJ13 (SDS-resistant tetramer shown) in $Spak^{+/+}$ and $Spak^{-/-}$ rat ChP. (E) Representative IHC co-staining of pSPAK (red) with ATP1A1 (green, top row), KCNJ13 (green, second row), CLIC6 (green, third row), and AQP1 (green, last row) in ChP of WT, $Spak^{-/-}$, and $Tlr4^{-/-}$ animals +/− LPS treatment (n=6 ChP per genotype, 3 animals per condition). Insets show
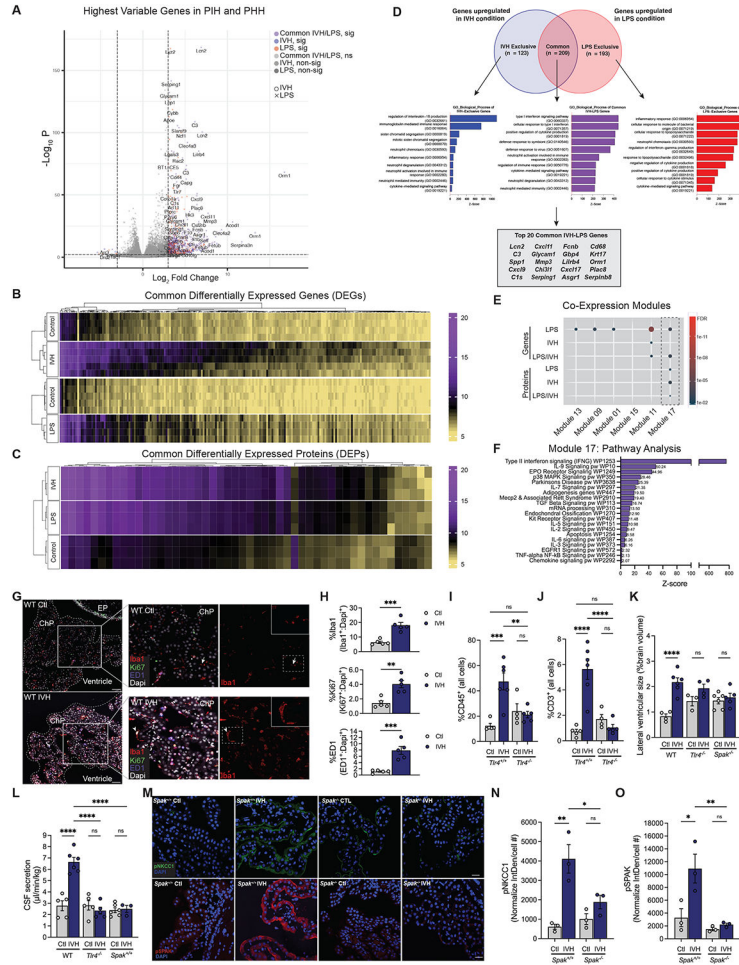
magnification; apical membrane (Ap), basolateral membrane (Bl) of the choroid plexus. 40x, Scale bars 25 μm.

Figure 4. Post-hemorrhagic and -infectious hydrocephalus models exhibit highly similar ChP immune-secretory pathophysiology.

(A) Volcano plot and heatmaps of the most highly significant (sig) (B) DEGs and (C) DEPs compared to control from bulk RNAseq analyses of ChP from Ctl, IVH, and LPS-treated animals (n=3-5 animals per condition). (D) Venn diagram and GO biological process analysis of genes upregulated in IVH versus LPS conditions, and those common to both conditions. Outlined box at the bottom shows the top 20 DEGs common to IVH and LPS. (E) Hypergeometric enrichment analysis of gene co-expression modules for DEG/DEPs between LPS and IVH, and shared (LPS/IVH) DEG/DEPs (dashed box highlights shared enrichment in Module 17). (F) Module 17 pathway analysis. (G) Representative IHC of Iba1 (red), Ki67 (green), and ED1 (blue) cells in ChP of Ctl and IVH-treated rats (n=5 animals per condition) (ChP border denoted by dashed white outline; EP, ependyma). Left panel inset, ChP magnification; right panel inset, magnification Iba1$^+$ cell (white arrows). Scale bars, 50µm. (H) Quantitative IHC in (G) showing % (normalized to DAPI) of ED1$^+$, Ki67$^+$, and Iba1$^+$ cells (n=5 animals per condition). (I, J) FACS quantification of (I) CD45$^+$ and (J) CD3$^+$ cells in ChP from IVH-treated *Tlr4*$^{+/+}$ and *Tlr4*$^{-/-}$ rats (n=4-6 animals per condition). (K) Quantitation of lateral ventricular size (% brain volume) and (L) body weight-normalized CSF secretion in WT, *Tlr4*$^{-/-}$, and *Spak*$^{-/-}$ IVH-treated (48h) rats (n=3-6 animals per condition). (M) Representative ChP IHC of pNKCC1 (green) and pSPAK

(red) expression in Ctl and IVH-treated $Spak^{+/+}$ and $Spak^{-/-}$ animals. Scale bars, 25 μm. Quantitation of (N) pNKCC1 (Interval Density/cell #) and (R) pSPAK IHC in (O) (n=6 ChP, 3 animals per condition). Error bars, mean ±sem; each symbol represents one animal. *p<0.05, **p<0.01, ***p<0.001, ****p<0.0001, ns = not significant; unpaired t-test (K) or one-way ANOVA (L-O, Q, R). [D-G, abbreviations: pos reg = positive regulation, neg reg = negative regulation, pw = pathway, act = activity, a/o = acting on, FA = focal adhesion, Mϕ = macrophage].
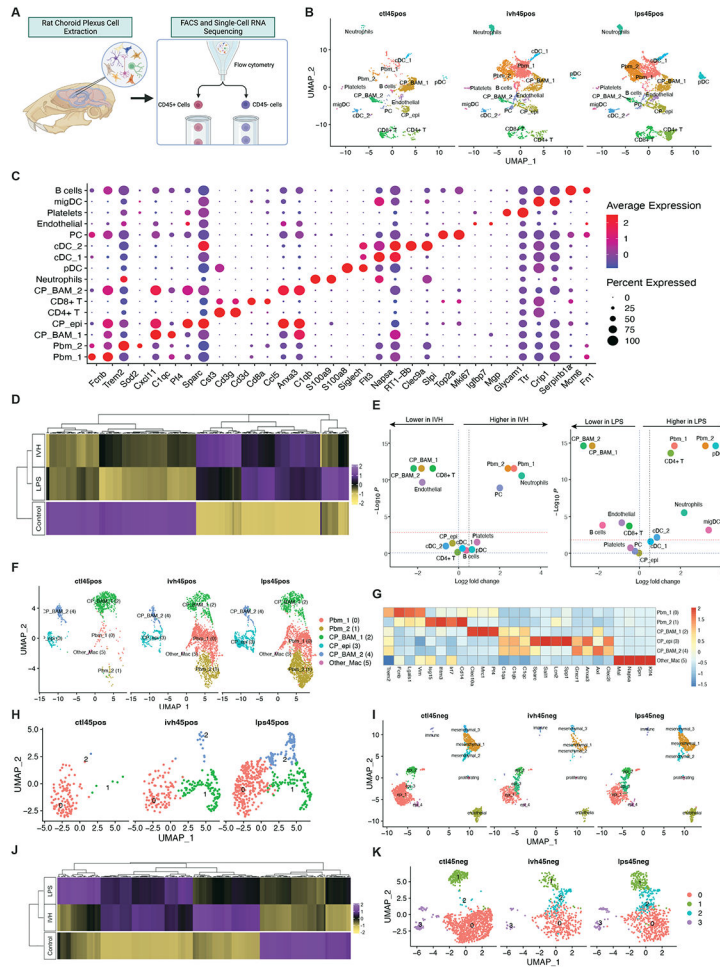
Figure 5. scRNAseq uncovers crosstalk between peripheral and resident immune cells and epithelial cells at the ChP.

(A) Schematic illustrating the scRNA experimental design and downstream analyses.

(B) UMAP clustering of ChP CD45$^+$ cells across control, IVH-treated and LPS-treated conditions, colored by cell type. (C) DotPlot showing gene expression signatures of CD45$^+$ cell clusters, with dot size representing the percentage of cells expressing the gene and the color representing average expression within a cluster. (D) Heatmap of the top differentially expressed genes (DEGs) comparing ChP CD45$^+$ cell expression profiles from Ctl, IVH, and LPS-treated animals. (E) Volcano plots depicting differences of cluster abundance in IVH-treated and LPS-treated ChP CD45$^+$ cells compared to control plotting fold change (log10) against p-value (−log10) based on beta-binomial regression. The red horizontal dashed line indicates the significance threshold. (F) UMAP of ChP myeloid cell clusters, including peripheral blood macrophages, CP stromal macrophages and CP epiplexus macrophages, colored by cell type. (G) Heatmap of the top DEGs for myeloid subclusters. (H) UMAP of ChP epiplexus macrophage subclusters, colored by group, showing transformed and proliferating epiplexus macrophages in control, IVH, and LPS conditions. (I) UMAP clustering of ChP CD45$^−$ cells across IVH-treated, LPS-treated, and control conditions, colored by cell type. (J) Heatmap of top DEGs comparing ChP CD45$^−$ epithelial cell
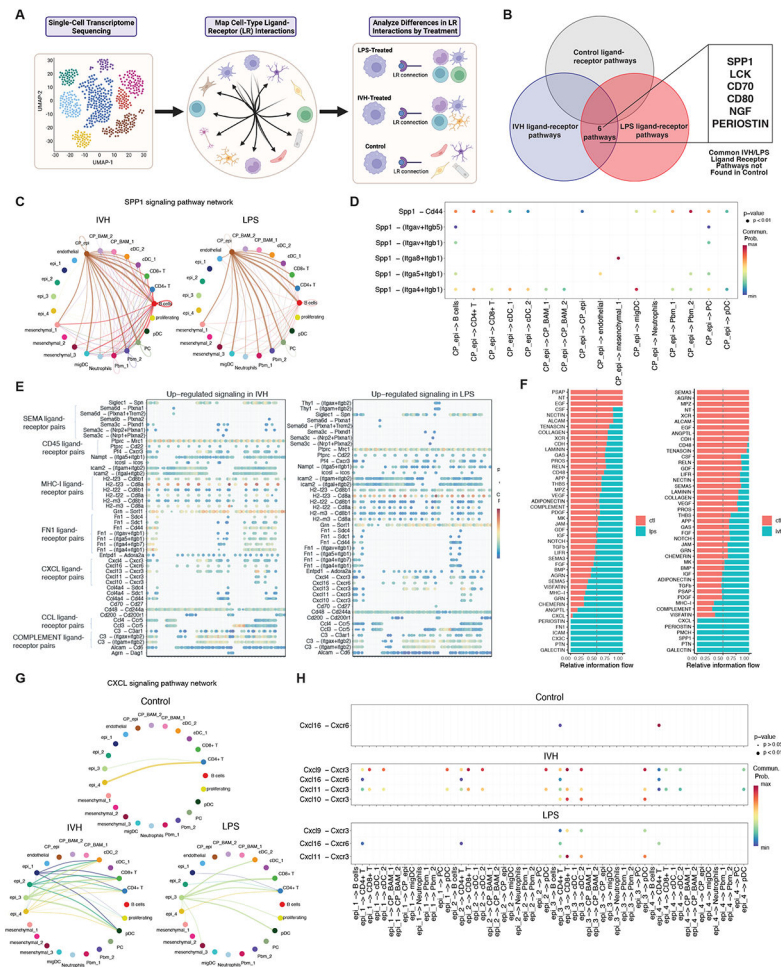
expression profiles from Ctl, IVH, and LPS-treated animals. (K) UMAP of ChP epithelial subclusters, colored by group.

Figure 6. scRNAseq CellChat analysis reveals ligand-receptor pairs enabling ChP immune-epithelial cell communication.

(A) Schematic illustrating CellChat downstream analyses. (B) Identification of 6 ligand-receptor pathways shared between IVH-treated and LPS-treated rats and absent in control. (C) Circle plot depicting ligand-receptor interactions of the SPP1 pathway in IVH-treated and LPS-treated ChP. Edge width represents communication probability. (D) Bubble plot showing significant ligand-receptor interactions for the SPP1 pathway in IVH-treated and LPS-treated ChP (no significant interactions were found for control). X-axis shows the cell groups associated with the interactions. Y-axis shows the ligand-receptor pairs. Dot color reflects communication probabilities and dot size represents computed p-values. Empty space means zero communication probability. p-values reflect a one-sided permutation test. (E) Upregulated ligand-receptor pairs for IVH-treated and LPS-treated ChP compared to control, showing significant overlap of upregulated pathways in IVH and LPS, with increased signal in SEMA, CD45, MHC-I, FN1, CXCL, CCL, COMPLEMENT pathway ligand-receptor pairs for both conditions. Dot color reflects communication probabilities and dot size represents computed p-values (from a one-sided permutation test). (F) Significant signaling pathways ranked based on differences in the overall information flow within the inferred networks between epithelial and CD45^{+} cells, comparing LPS (left) and IVH conditions (right) to control. The overall information flow of a signaling network

is calculated by summarizing all communication probabilities in that network. Rows with high blue-to-red ratio indicate higher ligand-receptor pathway activity for IVH or LPS conditions. (G) Circle plot comparing CXCL pathway ligand-receptor interactions among control, IVH-treated, and LPS-treated ChP epithelial and CD45$^+$ cell groups. Edge width represents communication probability. (H) Comparison of control, IVH, and LPS bubble plots showing significant ligand-receptor interactions between epithelial and CD45$^+$ cells for the CXCL pathway. X-axis shows the cell groups associated with the interactions. Y axis shows the ligand-receptor pairs. Dot color reflects communication probabilities, and dot size represents computed p-values (from a one-sided permutation test). Empty space means zero communication probability.
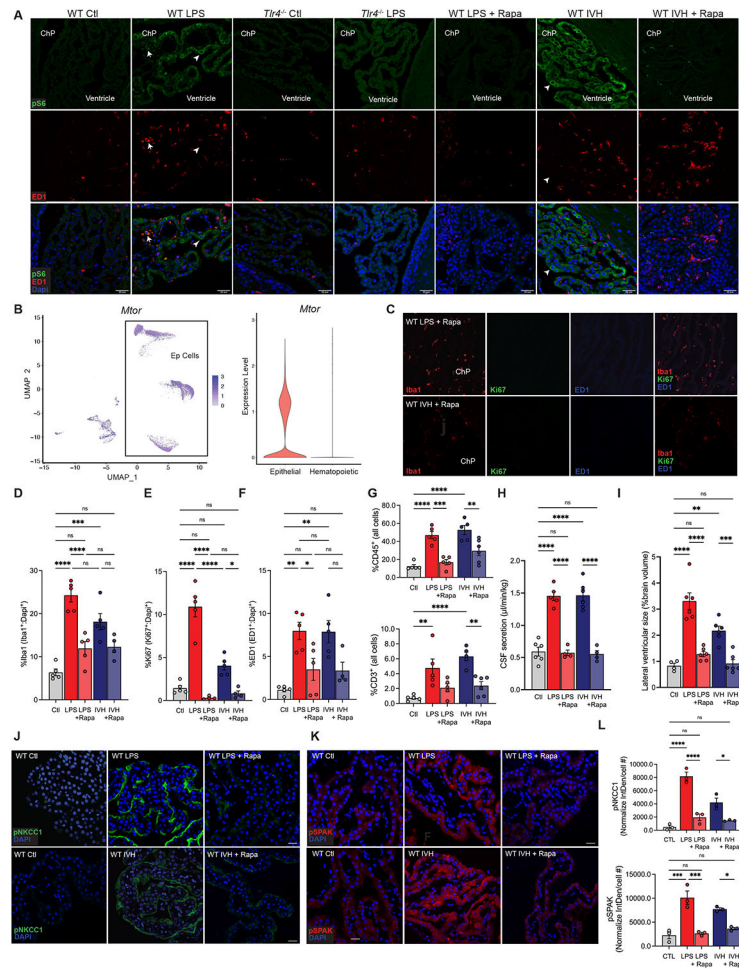
Figure 7. Repurposed systemic immunomodulators treat hydrocephalus by antagonizing ChP-mediated CSF hypersecretion.

(A) Representative IHC of pS6 (green) and ED1 (red) in ChP-associated immune cells (arrows) and epithelial cells (arrowheads) in WT and $Tlr4^{-/-}$ animals +/− LPS, and WT LPS and IVH conditions +/− Rapamycin (Rapa) (n=5). Scale bars, 30μm. DAPI, blue. (B) snRNAseq analysis (left panel) and violin plot (right) demonstrating $Mtor$ in ChP epithelial (Ep) cells and ChP-associated hematopoietic cells (Epithelial, Avg Log$_2$FC=7.88e-2, p=1.23e-17). (C) Representative IHC of Iba1 (red), Ki67 (red), and ED1 (blue) expression in the ChP of WT rats treated with LPS or IVH, in the presence of Rapa. (D-F) Quantitative IHC of the ChP immune response in (C) in WT LPS and IVH-treated animals +/−Rapa. Graphs represent DAPI-normalized % of cells identified as (D) Iba1$^+$, (E) Ki67$^+$, (F) ED1$^+$ in Ctl, LPS, LPS+Rapa, IVH, and IVH+Rapa-treated animals (n=4-6). (G) Quantitation of FACS-isolated CD45$^+$ and CD3$^+$ cells in Ctl, LPS, LPS+Rapa, IVH, IVH+Rapa-treated rats (n=5-6). (H) Weight-normalized CSF secretion and (I) lateral ventricular size (% brain volume) in Ctl, LPS, LPS+Rapa, IVH, and IVH+Rapa-treated animals (n=4-6). Representative IHC of (J) pNKCC1 and (K) pSPAK expression in WT Ctl, LPS +/−Rapa, and IVH +/−Rapa. (L) Quantitation (Interval Density/cell #) of pNkcc1 and pSPAK IHC in (J) and (K), respectively (n=6 ChP, 3 animals). Error bars, mean ± sem; each symbol

represents one animal. *p<0.05, **p<0.01, ***p<0.001, ****p<0.0001, ns = not significant; one-way ANOVA.

Key resources table

REAGENT or RESOURCE	SOURCE	IDENTIFIER
Antibodies		
AQP1, rabbit recombinant monoclonal	Abcam	Ab168387
ATP1A, rabbit polyclonal	Alomone	ANP-001
CD68, rabbit monoclonal	CST	97778
CLIC6, mouse monoclonal	Santa Cruz	365303
ED1/CD68, mouse monoclonal	Millipore	MAB1435
IBA1, goat polyclonal	Thermo	PA5-18039
KCNJ13, mouse monoclonal	Santa Cruz	398810
Ki67, rabbit monoclonal	CST	9129
pNKCC1, rabbit polyclonal	Millipore	ABS 1004
pSPAK, rabbit polyclonal	Millipore	07-2273
RELT, rabbit polyclonal	Novus	NBP2-56851
NKCC1, rabbit monoclonal	CST	85403S
Anti-WNK1	University of Dundee	S079B
Anti-SPAK	University of Dundee	S365D
Anti-NKCC1	University of Dundee	S022D
Anti-ATP1A1	DSHB	a5
Anti-HRP	Pierce	21130
Anti-beta actin	Abcam	Ab8227
CD16-32	Biolegend	Cat#: 101302
CD45-PE/cy7	Biolegend	Cat#: 202207
CD3-647	Biolegend	Cat#: 201408
Alexa Fluor 488	Invitrogen	Cat#: A32723
Alexa Fluor 555	Invitrogen	Cat#: A32816
Alexa Fluor 647	Invitrogen	Cat#: A32849
Bacterial and virus strains		
E. Coli^{+LPS} (BD21)	Lucigen	*E. cloni* EXPRESS BL21(DE3)
E. Coli^{-LPS} (ClearColi)	Lucigen	CLEARCOLI BL21
Biological samples		
N/A		
Chemicals, peptides, and recombinant proteins		

REAGENT or RESOURCE	SOURCE	IDENTIFIER
Bumetanide	Sigma-Aldrich	CAS#: 28395-03-1
aCSF	Harvard Apparatus	Item#: 59-7316
Rapamycin	Cayman	Item#: 13346
Critical commercial assays		
N/A		
Deposited data		
Bulk RNA seq	GEO	GSE192946
Mass spectrometry proteomics data	PRIDE	PXD030678
ScRNA seq	GEO	GSE218143
Experimental models: Cell lines		
N/A		
Experimental models: Organisms/strains		
Wistar rats, albino	Charles River	Strain code 003
Oligonucleotides		
N/A		
Recombinant DNA		
N/A		

REAGENT or RESOURCE	SOURCE	IDENTIFIER
Software and algorithms		
Seurat	Hao et al.[151]	https://satijalab.org/seurat/
Monocle3	Cao et al.[152]	https://cole-trapnelllab.github.io/monocle3/
Cellchat	Jin et al.[82]	https://github.com/sqjin/CellChat
Other		
N/A		

LIFE SCIENCE TABLE WITH EXAMPLES FOR AUTHOR REFERENCE

REAGENT or RESOURCE	SOURCE	IDENTIFIER
Antibodies		
Rabbit monoclonal anti-Snail	Cell Signaling Technology	Cat#3879S; RRID: AB_2255011
Mouse monoclonal anti-Tubulin (clone DM1A)	Sigma-Aldrich	Cat#T9026; RRID: AB_477593
Rabbit polyclonal anti-BMAL1	This paper	N/A
Bacterial and virus strains		
pAAV-hSyn-DIO-hM3D(Gq)-mCherry	Krashes et al.[1]	Addgene AAV5; 44361-AAV5
AAV5-EF1a-DIO-hChR2(H134R)-EYFP	Hope Center Viral Vectors Core	N/A
Cowpox virus Brighton Red	BEI Resources	NR-88
Zika-SMGC-1, GENBANK: KX266255	Isolated from patient (Wang et al.[2])	N/A
Staphylococcus aureus	ATCC	ATCC 29213
Streptococcus pyogenes: M1 serotype strain: strain SF370; M1 GAS	ATCC	ATCC 700294
Biological samples		
Healthy adult BA9 brain tissue	University of Maryland Brain & Tissue Bank; http://medschool.umaryland.edu/btbank/	Cat#UMB1455
Human hippocampal brain blocks	New York Brain Bank	http://nybb.hs.columbia.edu/
Patient-derived xenografts (PDX)	Children's Oncology Group Cell Culture and Xenograft Repository	http://cogcell.org/
Chemicals, peptides, and recombinant proteins		
MK-2206 AKT inhibitor	Selleck Chemicals	S1078; CAS: 1032350-13-2
SB-505124	Sigma-Aldrich	S4696; CAS: 694433-59-5 (free base)
Picrotoxin	Sigma-Aldrich	P1675; CAS: 124-87-8
Human TGF-β	R&D	240-B; GenPept: P01137
Activated S6K1	Millipore	Cat#14-486
GST-BMAL1	Novus	Cat#H00000406-P01
Critical commercial assays		
EasyTag EXPRESS 35S Protein Labeling Kit	PerkinElmer	NEG772014MC
CaspaseGlo 3/7	Promega	G8090
TruSeq ChIP Sample Prep Kit	Illumina	IP-202-1012
Deposited data		
Raw and analyzed data	This paper	GEO: GSE63473
B-RAF RBD (apo) structure	This paper	PDB: 5J17
Human reference genome NCBI build 37, GRCh37	Genome Reference Consortium	http://www.ncbi.nlm.nih.gov/projects/genome/assembly/grc/human/
Nanog STILT inference	This paper; Mendeley Data	http://dx.doi.org/10.17632/wx6s4mj7s8.2
Affinity-based mass spectrometry performed with 57 genes	This paper; Mendeley Data	Table S8; http://dx.doi.org/10.17632/5hvpvspw82.1

REAGENT or RESOURCE	SOURCE	IDENTIFIER
Experimental models: Cell lines		
Hamster: CHO cells	ATCC	CRL-11268
D. melanogaster: Cell line S2: S2-DRSC	Laboratory of Norbert Perrimon	FlyBase: FBtc0000181
Human: Passage 40 H9 ES cells	MSKCC stem cell core facility	N/A
Human: HUES 8 hESC line (NIH approval number NIHhESC-09-0021)	HSCI iPS Core	hES Cell Line: HUES-8
Experimental models: Organisms/strains		
C. elegans: Strain BC4011: srl-1(s2500) II; dpy-18(e364) III; unc-46(e177)rol-3(s1040) V.	Caenorhabditis Genetics Center	WB Strain: BC4011; WormBase: WBVar00241916
D. melanogaster: RNAi of Sxl: y[1] sc[*] v[1]; P{TRiP.HMS00609}attP2	Bloomington Drosophila Stock Center	BDSC:34393; FlyBase: FBtp0064874
S. cerevisiae: Strain background: W303	ATCC	ATTC: 208353
Mouse: R6/2: B6CBA-Tg(HDexon1)62Gpb/3J	The Jackson Laboratory	JAX: 006494
Mouse: OXTRfl/fl: B6.129(SJL)-Oxtr$^{tm1.1Wsy}$/J	The Jackson Laboratory	RRID: IMSR_JAX:008471
Zebrafish: Tg(Shha:GFP)t10: t10Tg	Neumann and Nuesslein-Volhard[3]	ZFIN: ZDB-GENO-060207-1
Arabidopsis: 35S::PIF4-YFP, BZR1-CFP	Wang et al.[4]	N/A
Arabidopsis: JYB1021.2: pS24(AT5G58010)::cS24:GFP(-G):NOS #1	NASC	NASC ID: N70450
Oligonucleotides		
siRNA targeting sequence: PIP5K I alpha #1: ACACAGUACUCAGUUGAUA	This paper	N/A
Primers for XX, see Table SX	This paper	N/A
Primer: GFP/YFP/CFP Forward: GCACGACTTCTTCAAGTCCGCCATGCC	This paper	N/A
Morpholino: MO-pax2a GGTCTGCTTTGCAGTGAATATCCAT	Gene Tools	ZFIN: ZDB-MRPHLNO-061106-5
ACTB (hs01060665_g1)	Life Technologies	Cat#4331182
RNA sequence: hnRNPA1_ligand: UAGGGACUUAGGGUUCUCUCUAGGGACUUAG GGUUCUCUCUAGGGA	This paper	N/A
Recombinant DNA		
pLVX-Tight-Puro (TetOn)	Clonetech	Cat#632162
Plasmid: GFP-Nito	This paper	N/A
cDNA GH111110	Drosophila Genomics Resource Center	DGRC:5666; FlyBase:FBcl0130415
AAV2/1-hsyn-GCaMP6-WPRE	Chen et al.[5]	N/A
Mouse raptor: pLKO mouse shRNA 1 raptor	Thoreen et al.[6]	Addgene Plasmid #21339
Software and algorithms		
ImageJ	Schneider et al.[7]	https://imagej.nih.gov/ij/
Bowtie2	Langmead and Salzberg[8]	http://bowtie-bio.sourceforge.net/bowtie2/index.shtml
Samtools	Li et al.[9]	http://samtools.sourceforge.net/
Weighted Maximal Information Component Analysis v0.9	Rau et al.[10]	https://github.com/ChristophRau/wMICA

REAGENT or RESOURCE	SOURCE	IDENTIFIER
ICS algorithm	This paper; Mendeley Data	http://dx.doi.org/ 10.17632/5hvpvspw82.1
Other		
Sequence data, analyses, and resources related to the ultra-deep sequencing of the AML31 tumor, relapse, and matched normal	This paper	http://aml31.genome.wustl.edu
Resource website for the AML31 publication	This paper	https://github.com/chrisamiller/ aml31SuppSite

PHYSICAL SCIENCE TABLE WITH EXAMPLES FOR AUTHOR REFERENCE

REAGENT or RESOURCE	SOURCE	IDENTIFIER
Chemicals, peptides, and recombinant proteins		
QD605 streptavidin conjugated quantum dot	Thermo Fisher Scientific	Cat#Q10101MP
Platinum black	Sigma-Aldrich	Cat#205915
Sodium formate BioUltra, 99.0% (NT)	Sigma-Aldrich	Cat#71359
Chloramphenicol	Sigma-Aldrich	Cat#C0378
Carbon dioxide (^{13}C, 99%) (<2% ^{18}O)	Cambridge Isotope Laboratories	CLM-185-5
Poly(vinylidene fluoride-co-hexafluoropropylene)	Sigma-Aldrich	427179
PTFE Hydrophilic Membrane Filters, 0.22 μm, 90 mm	Scientificfilters.com/TischScientific	SF13842
Critical commercial assays		
Folic Acid (FA) ELISA kit	Alpha Diagnostic International	Cat# 0365-0B9
TMT10plex Isobaric Label Reagent Set	Thermo Fisher	A37725
Surface Plasmon Resonance CM5 kit	GE Healthcare	Cat#29104988
NanoBRET Target Engagement K-5 kit	Promega	Cat#N2500
Deposited data		
B-RAF RBD (apo) structure	This paper	PDB: 5J17
Structure of compound 5	This paper; Cambridge Crystallographic Data Center	CCDC: 2016466
Code for constraints-based modeling and analysis of autotrophic *E. coli*	This paper	https://gitlab.com/elad.noor/sloppy/tree/master/rubisco
Software and algorithms		
Gaussian09	Frish et al.[1]	https://gaussian.com
Python version 2.7	Python Software Foundation	https://www.python.org
ChemDraw Professional 18.0	PerkinElmer	https://www.perkinelmer.com/category/chemdraw
Weighted Maximal Information Component Analysis v0.9	Rau et al.[2]	https://github.com/ChristophRau/wMICA
Other		
DASGIP MX4/4 Gas Mixing Module for 4 Vessels with a Mass Flow Controller	Eppendorf	Cat#76DGMX44
Agilent 1200 series HPLC	Agilent Technologies	https://www.agilent.com/en/products/liquid-chromatography
PHI Quantera II XPS	ULVAC-PHI, Inc.	https://www.ulvac-phi.com/en/products/xps/phi-quantera-ii/